Design principles governing the motility of myosin V

Michael Hinczewski[a,1], Riina Tehver[b], and D. Thirumalai[a,1]

[a]Biophysics Program, Institute for Physical Science and Technology, University of Maryland, College Park, MD 20742; and [b]Department of Physics and Astronomy, Denison University, Granville, OH 43023

Edited* by James A. Spudich, Stanford University School of Medicine, Stanford, CA, and approved August 28, 2013 (received for review June 30, 2013)

The molecular motor myosin V (MyoV) exhibits a wide repertoire of pathways during the stepping process, which is intimately connected to its biological function. The best understood of these is the hand-over-hand stepping by a swinging lever arm movement toward the plus end of actin filaments. Single-molecule experiments have also shown that the motor "foot stomps," with one hand detaching and rebinding to the same site, and back-steps under sufficient load. The complete taxonomy of MyoV's load-dependent stepping pathways, and the extent to which these are constrained by motor structure and mechanochemistry, are not understood. Using a polymer model, we develop an analytical theory to describe the minimal physical properties that govern motor dynamics. We solve the first-passage problem of the head reaching the target-binding site, investigating the competing effects of backward load, strain in the leading head biasing the diffusion in the direction of the target, and the possibility of preferential binding to the forward site due to the recovery stroke. The theory reproduces a variety of experimental data, including the power stroke and slow diffusive search regimes in the mean trajectory of the detached head, and the force dependence of the forward-to-backward step ratio, run length, and velocity. We derive a stall force formula, determined by lever arm compliance and chemical cycle rates. By exploring the MyoV design space, we predict that it is a robust motor whose dynamical behavior is not compromised by reasonable perturbations to the reaction cycle and changes in the architecture of the lever arm.

functional robustness | polymer physics | architectural basis | stall force expression

Myosin V (MyoV), a cytoskeletal motor protein belonging to the myosin superfamily (1), converts energy from ATP hydrolysis into the transport of intracellular cargo, such as mRNA and organelles along actin filaments (2). In its dimeric form, the motor has two actin-binding, ATPase heads connected to α-helical lever arm domains stiffened by attached calmodulins or essential light chains (Fig. 1). The nucleotide-driven mechanochemical cycle of the heads produces two changes in the lever arm orientation: a power stroke, where an actin-bound head swings the lever arm forward toward the plus (barbed) end of the filament, and a recovery stroke, which returns the arm to its original configuration when the head is detached from actin (3). The motor translates these changes into processive plus end-directed movement (4–6). By alternating head detachment, MyoV walks hand-over-hand (7, 8), taking one step of ≈36 nm for each ATP consumed (9). At small loads, the motor can complete ≈20 – 60 forward steps before dissociating from actin (6, 10, 11). Such a high unidirectional processivity requires coordination in the detachment of the two heads, a "gating" mechanism, which is believed to arise from the strain within the molecule when both heads are bound to actin (12–15). Sufficiently large opposing loads can counteract the plus end-directed bias, resulting in an increase in the probability of back-stepping (16) until the motor velocity goes to zero at a stall force of ≈1.9 – 3 pN (4, 12, 16–19). Although MyoV is among the most extensively studied motor proteins, improvements in experimental resolution continue to provide new and surprising insights into the details of its dynamics. A beautiful recent example is the high-speed atomic force microscopy (AFM) of Kodera et al. (20), which was used to visualize not only the expected hand-over-hand stepping but additional, less well-understood processes like "foot stomping" (21, 22), where one head detaches and rebinds to the same site. Thus, a comprehensive picture of MyoV motility needs to account for all the kinetic pathways, including back-stepping and foot stomping, how they vary under load, and their relationship to the structural and chemical parameters of the motor.

To address these issues, we introduce a minimal model of MyoV dynamics, focusing on the stochastic fluctuations of the motor head during the diffusive search of the detached head for a binding site, whose importance has been illuminated by various experiments (22–25). The large persistence length l_p of the lever arms (26–28) allows us to propose a coarse-grained polymer model for the reaction-diffusion problem, which, in turn, yields approximate analytical expressions for all the physical observables, including binding times, run length, velocity, and stall force. We have built on the insights of earlier theoretical works (28–34), which focused on modeling a reaction network of discrete states in the mechanochemical cycle of the motor heads. Our work supplements the reaction network with an explicit treatment of the diffusive search, which has been studied using insightful Brownian dynamics simulations of forward stepping in MyoV (35). An important aspect of our theory is that it allows us to tackle not just forward steps but the full complexity of foot stomping and back-stepping across the entire force spectrum up to the stall point. In our framework, the load dependence of the MyoV behavior enters naturally, because pulling on the molecule shifts the speed and likelihood of the detached head reaching the forward or backward binding site. The competition between the time scales of first passage to the sites, and how they compare with the detachment rates of the heads, determines the partitioning of the kinetic pathways. Significantly, polymer theory gives us a direct connection between the kinetics and the structural features of the motor, like the bending elasticity of the lever arms and the orientational bias due to the power stroke. The result is a theory with only three fitting parameters that have not been previously determined through experiment, all of which have simple physical interpretations. The theoretical fit quanti-

Significance

Myosin V, a two-headed motor protein, ferries cellular cargo by walking hand-over-hand on actin filaments. Interplay between ATP-driven conformational changes in the heads and stress due to load produces a variety of stepping dynamics: The motor can step forward or backward, or "stomp," where one head detaches and rebinds to the same site. We created an analytically solvable theory capturing all these behaviors, quantitatively matching a wide array of single-molecule experiments. We describe the structural and chemical design principles underlying the motor's robust function, providing a guide for how bioengineering might alter its dynamics.

Author contributions: M.H. and D.T. designed research; M.H. and R.T. performed research; M.H., R.T., and D.T. analyzed data; and M.H. and D.T. wrote the paper.

The authors declare no conflict of interest.

*This Direct Submission article had a prearranged editor.

[1]To whom correspondence may be addressed. E-mail: mhincz@gmail.com or dave.thirumalai@gmail.com.

This article contains supporting information online at www.pnas.org/lookup/suppl/doi:10.1073/pnas.1312393110/-/DCSupplemental.

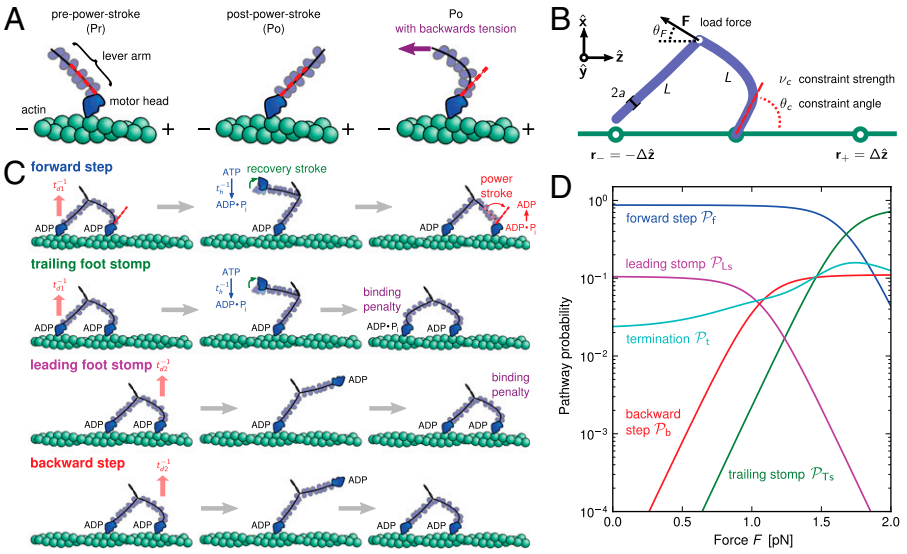

Fig. 1. (*A*) Orientational states of the MyoV head with respect to its lever arm. For clarity, only one leg of the two-legged motor is shown, although the states are the same for both legs. (*Left*) Pr. (*Middle*) Po. For each state, the relaxed orientation (in the absence of tension on the lever arm end) is marked by a dashed red line. (*Right*) Po state with backward tension on the arm end, causing the lever arm to bend backward away from its relaxed direction. (*B*) Coarse-grained polymer representation of MyoV. (*C*) Schematic view of four MyoV kinetic pathways. For simplicity, the nucleotide-free state, following ADP release from the TH and before ATP binding, is not shown. (*D*) Probability of each kinetic pathway as a function of backward force F (with $\theta_F = 0$) calculated from the theory using the parameter set in Table 1.

tatively reproduces a variety of experimental data, like the time-dependent mean trajectories of the detached head (23) and the force dependence of the backward-to-forward step ratio (16) and run length/velocity (4, 16–18, 36). We also explore more broadly the design space of MyoV structural parameters, allowing us to predict the essential requirements for the observed dynamical behavior and to answer the following questions. Is the structure of the motor dictated by certain natural constraints? How robust is the motility of MyoV to perturbations in the parameters? What are the relative contributions of head chemistry (resulting from changes in the nucleotide states) and the structural features to the measured stall force? The answers to these questions, which are provided in terms of phase diagrams, lead to testable predictions.

Results

Polymer Model for MyoV. In our model for MyoV (Fig. 1*B*), the motor and lever arm domains of each head are represented as a single semiflexible polymer chain with contour length L and persistence length l_p. The two polymer legs are connected at a freely rotating joint. The parameter values characterizing our model are listed in Table 1. Although the tail domain of MyoV, attached to the cargo, is not explicitly included, its effect is to transmit a load force $\mathbf{F}$ to the joint. The force is oriented in the $\hat{\mathbf{x}}-\hat{\mathbf{z}}$ plane, at an angle θ_F, measured clockwise from $-\hat{\mathbf{z}}$. The axis $\hat{\mathbf{z}}$ runs parallel to the actin filament, pointing toward the plus end. Our focus here is to study backward or resistive load ($0 \le \theta_F < 90°$) at force magnitudes smaller or close to the stall, $F \lesssim F_{\text{stall}} \approx 1.9-3$ pN (4, 12, 16–19). The polymer end points can bind to the actin filament at discrete binding sites, which are evenly spaced at a distance $\Delta = 36$ nm along the filament, corresponding approximately to the half-pitch of the actin double-helical structure (13 G-actin subunits). Although the model can be extended to incorporate a distribution of Δ values, reflecting binding to subunits neighboring the primary binding sites, in the simplest approximation, we keep Δ fixed. Because the first passage times to the primary binding site and its neighbors are similar, the effect of this approximation is small.

For each leg, the lever arm can adopt different preferred configurations with respect to the motor head during the course of the stepping cycle: the prepower-stroke (Pr) and postpower-stroke (Po) states. When the motor head is bound to actin and there is no tension on the end of the lever arm transmitted through the junction, the two states have relaxed configurations, as illustrated in Fig. 1*A* (*Left* and *Middle*). In the Pr state, the lever arm relaxes to an orientation tilting toward the actin-minus end, whereas in the Po state, it tilts toward the actin-plus end. In our model, the tilting preference of the Po state enters as a harmonic constraint on the end tangent of the bound leg: If $\hat{\mathbf{u}}_0$ is the unit tangent vector at the point where the polymer leg attaches to actin, we have a potential of $\mathcal{H}_c = \frac{1}{2} k_B T \nu_c (\hat{\mathbf{u}}_0 - \hat{\mathbf{u}}_c)^2$, with a constraint strength ν_c and direction $\hat{\mathbf{u}}_c$. Here, k_B is Boltzmann's constant, and T is temperature. The vector $\hat{\mathbf{u}}_c$ is in the $\hat{\mathbf{x}}-\hat{\mathbf{z}}$ plane at an angle $0 < \theta_c < \pi/2$, where θ_c is the constraint angle, measured counterclockwise from the $+\hat{\mathbf{z}}$ axis (the $\hat{\mathbf{u}}_c$ direction is marked by a red dashed line in Fig. 1 *A* and *B*). In principle, the Pr state is analogous but with distinct values of ν_c and θ_c, with the latter in the range of $\pi/2 < \theta_c < \pi$. However, as we will see below, all the kinetic pathways involve diffusion while the bound leg is in the Po state, so the parameters of the Pr state do not explicitly enter into the calculation. Hence, both ν_c and θ_c will refer only to the Po state.

If there is tension propagated through the junction on the end of the lever arm (i.e., due to load or to the fact that both motor heads are bound to actin), the lever arm contour will be bent away from its relaxed conformation. Fig. 1*A* (*Right*) shows the Po state under backward tension on the arm: The lever arm is bent, adopting a shape that reflects several competing physical effects. The Po constraint of strength ν_c tries to keep the head–arm angle near θ_c, the bending stiffness l_p favors a straight lever arm contour, and the tension tries to pull the end of the arm backward.

Table 1. MyoV model parameters

Parameter	Value	Notes
Mechanical parameters		
Leg contour length, L	35 nm	(35)
Leg persistence length, l_p	310 nm	(27)
Head diffusivity, D_h	5.7×10^{-7} cm^2/s	(40, 41)
Constraint angle, θ_c	60°	Fit to experiment (23)
Constraint strength, ν_c	184	Fit to experiment (16)
Binding parameters		
Binding site separation, Δ	36 nm	(35)
Capture radius, a	1 nm	
Binding penalty, b	0.065	Fit to experiment (6, 10, 11)
Chemical rates		
Hydrolysis rate, t_h^{-1}	750 s^{-1}	(38)
TH detachment rate, t_{d1}^{-1}	12 s^{-1}	(38)
LH detachment rate, t_{d2}^{-1}	1.5 s^{-1}	(15)
Gating ratio, $g = t_{d2}/t_{d1}$	8	

The polymer model naturally incorporates the interplay of these effects, which we will show is crucial in determining the dynamical response of the motor to load.

Kinetic Pathways. The starting point for all MyoV kinetic pathways (Fig. 1*C*, *Left*) is the waiting state, where both heads have ADP, are strongly bound to actin, and are in the Po state. Because the leading (L) leg is connected to the trailing (T) leg at the junction, the L leg is under backward tension, and it bends in the manner discussed above. The resulting strained "telemark" or "reverse arrowhead" stance has been observed directly in both EM (37) and AFM (20) images. The waiting state leads to four possible kinetic pathways (Fig. 1*C*).

1. Forward step. ADP is released from the trailing head (TH), followed by ATP binding, which makes association of the head with actin weak, leading to detachment. We assume saturating ATP concentrations (>100 μM), where ATP binding and subsequent TH detachment are very fast compared with ADP release; hence, the entire detachment process for the TH is modeled with a single rate of $t_{\mathrm{d1}}^{-1} = 12\ \mathrm{s}^{-1}$, equal to the experimentally measured ADP release rate (38). If we set the origin ($z = 0$) at the position of the bound leading head (LH), the free end of MyoV can diffuse and potentially rebind at one of two sites, $\mathbf{r}_{\pm} = \pm\Delta\hat{\mathbf{z}}$ along the actin filament (Fig. 1*B*). Binding at $\mathbf{r}_{+}$ leads to a forward step (Fig. 1*C*, row 1). However, successful binding is dependent on two conditions: (*i*) reaching the capture radius a around the binding site and (*ii*) the motor head having already hydrolyzed its bound ATP.

During the diffusive search, the entire two-legged polymer structure fluctuates in three dimensions, subject only to the end-tangent constraint at the bound leg attachment point. First passage to a given binding site $\mathbf{r}_{\pm}$, which occurs at a mean time interval $t_{\mathrm{fp}}^{\pm}$ after detachment, is the first arrival of the detached head to any point within a radius a of the binding site. The capture radius a, which reflects the distance at which the free MyoV head can appreciably interact with the actin-binding site (35), is set to $a = 1$ nm, comparable to the Debye screening length λ_D in physiological and in vitro conditions (i.e., for KCl concentrations of $25-400$ mM, $\lambda_D \approx 1.9-0.5$ nm).

The second condition for successful binding is the chemical state of the detached head. In order for the head to strongly associate and bind to actin, ATP must hydrolyze to ADP + inorganic phosphate ($\mathrm{P_i}$), which occurs at a hydrolysis rate of $t_{\mathrm{h}}^{-1} = 750\ \mathrm{s}^{-1}$ (38). Along with hydrolysis, the detached head also undergoes a recovery stroke, which reverses the power stroke, changing the orientation of the head with respect to the lever arm (Po→Pr). For simplicity, we combine the nucleotide/head–arm orientation states of the detached head into two possibilities: ATP/Po (A) and ADP + $\mathrm{P_i}$/Pr (B). Unless otherwise specified, we assume the transition A→B occurs irreversibly at a rate of t_{h}^{-1}. (We will discuss one experimental variant of MyoV with modified light chain composition in the section on zero load binding kinetics, where there is a nonnegligible reverse hydrolysis rate of $t_{-\mathrm{h}}^{-1}$). Binding can only occur in state B, so if the detached TH has reached the capture radius of one of the sites and the system is still in state A, it has a zero probability of binding, resulting in the TH continuing its diffusive trajectory. For forward stepping to occur, the TH must reach the capture radius of $\mathbf{r}_{+}$ in state B, and then it can bind with a probability of 1.

After successful binding, $\mathrm{P_i}$ is rapidly released from the bound head, which then results in a Pr→Po transition, returning the motor to its waiting state, with both the heads being in the Po state. Release of $\mathrm{P_i}$ and the power stroke is much faster than the detachment time scale t_{d1} (13), so we can assume that the motor with two bound heads spends nearly all its time waiting in the telemark stance.

2. T foot stomp. This kinetic pathway (Fig. 1*C*, row 2) is similar to the forward step, except that the detached TH diffuses to the site $\mathbf{r}_{-}$ rather than $\mathbf{r}_{+}$. Rebinding at $\mathbf{r}_{-}$ brings the center of mass of the motor back to its original location, without any net movement along the actin. For the binding to be successful, the head must be in state B within the capture radius a of $\mathbf{r}_{-}$, in which case it will bind with a probability of $b < 1$. The reduced probability of binding is a crucial difference between the forward step and T foot stomp pathways. The binding penalty b arises because the head in state B, after the recovery stroke, is in the Pr orientation, which is believed to favor binding to the forward target site ($\mathbf{r}_{+}$) over the backward site ($\mathbf{r}_{-}$) (3). Forward binding involves the detached head going in front of its lever arm, which has to tilt back toward the actin-minus end (the relaxed configuration of the Pr state). Backward binding has the opposite arrangement, with the lever arm bent toward the actin-plus end, which is an unnatural configuration in the Pr state, resulting in a strained back leg, as illustrated in Fig. 1*C* (*Right*), row 2. We model this effective extra energy barrier in the binding process through the probability b. The greater the barrier, the smaller is the value of b. The hypothesis that the recovery stroke is important in favoring forward binding has found support in a recent single-molecule study on single-headed MyoV (3), which established that the Pr orientation is highly kinetically and energetically stable (with an energy barrier of at least 5 k_BT with respect to Po).

3. L foot stomp. In addition to the two kinetic pathways above, initiated by TH detachment, there are two other possibilities that occur upon detachment of the LH. The first of these is the L foot stomp, where the LH unbinds and then rebinds to its original site (Fig. 1*C*, row 3). The detachment of the LH occurs at a slower rate than TH detachment, $t_{\mathrm{d2}}^{-1} = (g t_{\mathrm{d1}})^{-1}$, where we denote the factor $g > 1$ as the gating ratio. This asymmetry arises from the intramolecular strain within the two-legged MyoV structure bound to actin (12–15). The backward tension on the L lever arm in the waiting state slows down ADP release in the LH by 50- to 70-fold compared with the TH (13, 20), which makes detachment through the ADP-release/ATP-binding mechanism very rare. Rather, the LH under backward strain detaches primarily by means of an alternate pathway, where it retains ADP (15, 20), an assumption supported by the observation that single-headed MyoV under backward loads of ~ 2 pN unbinds from actin at a slow rate of $1.5\ \mathrm{s}^{-1}$ independent of both ATP and ADP concentrations (15). As described below, the magnitude of the backward tension in the waiting state can also be directly estimated from the structural parameters of the polymer model, giving a value of 2.7 pN, sufficient to be in the slow unbinding regime. Based on these considerations, we set $t_{\mathrm{d2}}^{-1} = 1.5\ \mathrm{s}^{-1}$ in our model, giving a gating ratio of $g = 8$. In other words, the TH is eightfold more likely to detach than the LH per unit time. We also assume the LH always retains ADP upon detachment [staying in the Po state (20)], and thus no ATP hydrolysis needs to occur before rebinding.

If we assign $z = 0$ to be the position of the bound TH, then the L foot stomp involves reattachment to its original site $\mathbf{r}_{+}$. Because the LH is Po, rebinding requires the lever arm to be bent backward, contrary to the plus-directed relaxed orientation of the Po state. We thus have a binding penalty analogous to the one for the T foot stomp: Successful binding will occur with a probability b within the capture radius a around $\mathbf{r}_{+}$. There is no additional chemical requirement, because the LH is in an ADP state with high affinity to actin. Although it is possible to assign a distinct binding penalty b for the T and L foot stomps, this does not lead to any major qualitative differences in the analysis below, so we assume, for simplicity, a single value of b. After binding, MyoV returns to the waiting state.

4. Backward step. The final kinetic pathway proceeds analogously to the L foot stomp, but the detached LH diffuses and binds to the backward site $\mathbf{r}_{-}$ (Fig. 1*C*, row 4). MyoV thus steps backward, shifting the center of mass toward the minus-end of actin. The detached head retains ADP and stays in the Po state. Because a forward-tilted lever arm is the relaxed conformation in the Po state, there is no binding penalty. Therefore, upon reaching the capture radius a around $\mathbf{r}_{-}$, the leg binds with a probability of 1, and MyoV returns to the waiting state. The fact that back-stepping in our model does not require ATP hydrolysis is consistent with observations of ATP-independent processive backward stepping in the superstall regime ($F > 3$ pN) (18). For simplicity, we will not

consider the superstall case in the present study. In principle, our model could be generalized to the superstall regime by including additional kinetic pathways that occur under extremely large backward loads, for example, power stroke reversal (39).

In all four kinetic pathways described above, only one leg is always bound to the actin during the diffusion step. If the bound leg detaches before the free leg binds, the processive run of MyoV is terminated. We assume a bound leg detachment rate of t_{d1}^{-1} during this process. This completes the description of the model, where each MyoV waiting state ends in five possible outcomes: forward stepping, T/L foot stomps, backward stepping, or detachment of both heads from actin. The first four pathways bring the system back to the waiting state, where the entire mechanochemical cycle can be repeated, whereas the last ends the run. The only parameters for which we do not have direct experimental estimates are the strength and direction of the power stroke constraint, ν_c and θ_c, respectively, and the binding penalty b. We will be able to fit these parameters by comparing the theoretical results with experimental data, as described below, resulting in the values listed in Table 1. Imaging studies (20, 37) suggest that the preferred Po orientation θ_c is likely to be in the vicinity of 60°, so this parameter could have been constrained from the outset. However, we have allowed it to be a free parameter because the angle θ_c that appears in the potential function $\mathcal{H}_c$ can, in principle, be slightly different from the observed orientation of the bound leg in any particular image, which is affected by both thermal fluctuations and any tension that is applied to the end of the bound leg. For the persistence length l_p, there are estimates ranging from $l_p \approx 100$ nm (26) up to $l_p \approx 375$ nm (28). We use the value $l_p = 310$ nm, based on the measurements of Moore et al. (27). From the point of view of the polymer model, the most important characteristic of the persistence length is that $l_p \gg L$, so the legs behave almost as rigid rods. However, one of the major outcomes of our theory is that precise tuning of the parameters is not required to get efficient processive dynamics qualitatively similar to those seen in nature.

Analytical Theory for Diffusive Search Times. The central physical quantity in our model is the first passage time to the binding site, $t_{\mathrm{fp}}^{\pm}$, which depends sensitively on the interplay of bending stiffness (l_p), load force (F, θ_F), and power stroke constraint (ν_c, θ_c) (Fig. 1*B*). The magnitude of $t_{\mathrm{fp}}^{\pm}$ at a given F compared with the t_{h}^{-1} and detachment rate, along with the size of the binding penalty, determines exactly how the system partitions among the various kinetic pathways.

Remarkably, the polymer model allows us to derive an approximate analytical expression for $t_{\mathrm{fp}}^{\pm}$ by exploiting the separation in time scales between polymer relaxation and the diffusive search (details are provided in *Materials and Methods* and *SI Text*). If t_{r} is the relaxation time for the two-legged polymer structure to equilibrate after one of the legs detaches, then $t_{\mathrm{r}} \ll t_{\mathrm{fp}}^{\pm}$. Theory and simulations show that $t_{\mathrm{r}} \approx 5$ μs for nearly rigid legs at zero load and that it becomes even smaller as F increases (Fig. 2). The value of t_{r} is two orders of magnitude smaller than the fastest times for first passage to the binding sites, $t_{\mathrm{fp}}^{\pm} \sim \mathcal{O}(0.1$ ms). Because $t_{\mathrm{fp}}^{\pm}/t_{\mathrm{r}} \gg 1$, we can relate $t_{\mathrm{fp}}^{\pm}$ to the distribution $\mathcal{P}(\mathbf{r})$, the probability density of finding the MyoV free end at position $\mathbf{r}$ once the system has reached equilibrium after leg detachment:

$$t_{\mathrm{fp}}^{\pm} \approx \frac{1}{4\pi D_{\mathrm{h}} a \mathcal{P}(\mathbf{r}_{\pm})}, \qquad [1]$$

where $D_{\mathrm{h}} = 5.7 \times 10^{-7}$ cm^2/s is the diffusion constant of the MyoV head, estimated using the program HYDROPRO (40) applied to the Protein Data Bank structure 1W8J (41). Eq. **1** transforms the dynamical problem of diffusive search time into one of calculating the equilibrium end-point distribution of a tethered, two-legged, semiflexible polymer structure. By adapting a mean field theory for individual semiflexible chains (42)

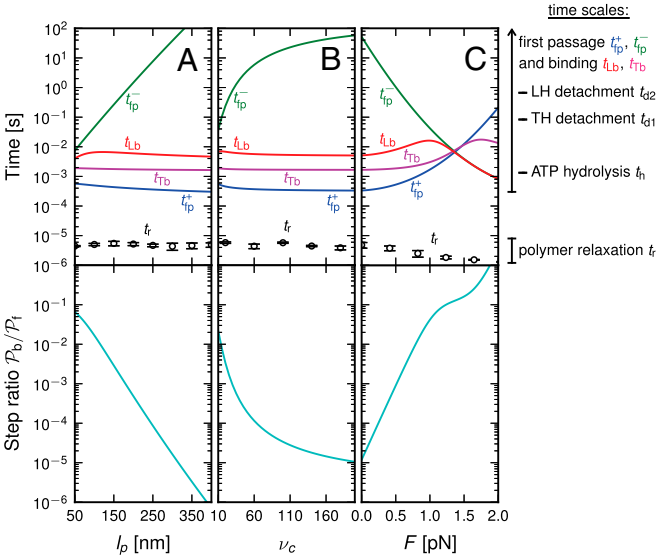

Fig. 2. (*Upper*) Theoretical predictions for the mean first passage time $t_{\mathrm{fp}}^{\pm}$ to the forward (+) and backward (–) sites; the mean binding times t_{Lb} and t_{Tb} for the L and T legs, respectively; and the polymer relaxation time t_{r} for the MyoV structure to equilibrate after the detachment of one leg. All results except t_{r} are derived from the analytical theory. The relaxation times are estimated using coarse-grained Brownian dynamics simulations (details are provided in *SI Text*). (*Right*) Main time scales in the problem are summarized, with their values (or ranges) indicated for comparison. (*Lower*) Ratio of backward to forward steps, $\mathcal{P}_{\mathrm{b}}/\mathcal{P}_{\mathrm{f}}$. For the three columns, the quantities are plotted as one parameter is varied, whereas all others are fixed at their Table 1 values: leg persistence length l_p (*A*), power stroke constraint strength ν_c (*B*), and load force F (with $\theta_F = 0$) (*C*).

and noting that contour fluctuations are small in the regime $l_p \gg L$, we obtained an approximate but accurate analytical expression for $\mathcal{P}(\mathbf{r}_{\pm})$, taking into account both the load force on the joint and the end-tangent constraint (*Materials and Methods* and *SI Text*). Together with Eq. **1**, we have a complete description of $t_{\mathrm{fp}}^{\pm}$ as a function of load and the MyoV structural parameters. If we assume that the other events in the mechanochemical cycle, hydrolysis and TH/LH detachment, are Poisson processes with respective rates of t_{h}^{-1}, t_{d1}^{-1}, and t_{d2}^{-1}, the probability of each kinetic pathway can also be derived, together with related quantities like mean run length and velocity. The full set of analytical equations for our model is summarized in *SI Text*.

Role of Diffusion in the Kinetic Pathway Probabilities at Zero Load. To gain an understanding of how the structural features of MyoV influence its motility, it is instructive to start with $F = 0$. Fig. 2 *A* (*Upper*) and *B* (*Upper*) shows the first passage times $t_{\mathrm{fp}}^{\pm}$ as a function of l_p and ν_c, respectively, with the other parameters being fixed at their Table 1 values. Because of the power stroke constraint, there is asymmetry in the first passage times: $t_{\mathrm{fp}}^{+} < t_{\mathrm{fp}}^{-}$ because the center of the $\mathcal{P}(\mathbf{r})$ distribution is shifted toward the forward binding site at $z = +\Delta$. At $F = 0$, the average z-axis location of the free leg, $\mu_z = \int dr (\hat{\mathbf{z}} \cdot \mathbf{r}) \mathcal{P}(\mathbf{r})$, is given by

$$\mu_z = l_p (1 - e^{-\kappa}) (\coth \nu_c - \nu_c^{-1}) \cos \theta_c, \qquad [2]$$

where $\kappa \equiv L/l_p$ and the origin $z = 0$ is at the binding site of the attached leg. With increasing l_p and ν_c, the position μ_z increases until it saturates at the limit of a rigid rod of length L with a fixed angle θ_c, $\mu_z \to L \cos \theta_c$. In this limit, $t_{\mathrm{fp}}^{-} \to \infty$, because it is geometrically impossible to reach the backward binding site $z = -\Delta$. In the opposite limit of small l_p and ν_c, the structure has greater flexibility, reaching the backward binding site is

easier, and the asymmetry is smaller. For $\nu_c \gg 1$ and $\kappa \ll 1$, the asymmetry parameter, $\alpha = t_{fp}^{+}/t_{fp}^{-}$, has a simple relationship to the structural parameters:

$$\alpha = \frac{t_{fp}^{+}}{t_{fp}^{-}} \approx \exp\left(-\frac{\Delta \mathcal{T}}{L}\cos\theta_c + \beta \Delta F \cos\theta_F\right),$$
$$\mathcal{T} \equiv 1 + \frac{20\nu_c}{20 + 7\kappa\nu_c}, \qquad [3]$$

where $\beta = 1/k_BT$ and $\Delta \approx 36$ nm is the step size. At $F = 0$, the key role in determining the degree of asymmetry is the factor $\mathcal{T}$, which depends on l_p and ν_c and is a dimensionless measure of the effectiveness of the power stroke constraint. A larger $\mathcal{T}$ means a smaller α and greater asymmetry. The form of $\mathcal{T}$ shows that the constraint strength ν_c by itself is insufficient to guarantee a large $\mathcal{T}$, because it can be counterbalanced by a small l_p. In other words, the end-tangent constraint does not have a significant effect if the polymer leg is too flexible. Thus, both ν_c and l_p have to be large to create significant asymmetry. In *Discussion*, we will highlight the relationship between $\mathcal{T}$ and important mechanical and energy scales in the system, including the overall compliance of the leg and the energy expended by the power stroke.

The asymmetry factor α influences kinetic pathway probabilities. At the end of each waiting stage, there is a probability of making a forward step ($\mathcal{P}_f$), a backward step ($\mathcal{P}_b$), an L foot stomp ($\mathcal{P}_{Ls}$), and a T foot stomp ($\mathcal{P}_{Ts}$). We plot these probabilities in Fig. 1*D* for a range of F. When the time scale of leg detachment is much larger than the binding times, the ratios of the pathway probabilities can be expressed in terms of α as

$$\frac{\mathcal{P}_b}{\mathcal{P}_f} = \frac{\alpha(1+b\alpha)}{g(b+\alpha)}, \qquad \frac{\mathcal{P}_{Ls}}{\mathcal{P}_f} = \frac{b(1+b\alpha)}{g(b+\alpha)}, \qquad \frac{\mathcal{P}_{Ts}}{\mathcal{P}_f} = b\alpha. \qquad [4]$$

Note that $\mathcal{P}_b/\mathcal{P}_f$ and $\mathcal{P}_{Ls}/\mathcal{P}_f$ are inversely proportional to g, the ratio of TH to LH detachment, which is expected because backward steps and L foot stomps can only occur when the LH detaches. The binding penalty b enters into all the ratios because it influences the likelihood of T/L foot stomping, which competes with the backward/forward stepping pathways. Fig. 2 *A* (*Lower*) and *B* (*Lower*) shows the variation of $\mathcal{P}_b/\mathcal{P}_f$ at $F = 0$ as l_p and ν_c are varied. We find that $\mathcal{P}_b/\mathcal{P}_f$ decreases as either variable increases, due to a larger $\mathcal{T}$ in Eq. **3**, resulting in a smaller α. Experimentally, MyoV exhibits negligible back-stepping at zero load, $\mathcal{P}_b/\mathcal{P}_f \lesssim 1\%$ (16). To achieve this extreme unidirectionality, $\mathcal{T}$ (or, equivalently, both ν_c and l_p) should be sufficiently large, an issue we will return to in *Discussion* when we examine the global constraints on the structural features of the motor. Along with back steps, T foot stomps are also negligible at $F = 0$ for small α, because $\mathcal{P}_{Ts}/\mathcal{P}_f \propto \alpha$. Because $\alpha \to 0$, the only ratio that has a nonzero limit is $\mathcal{P}_{Ls}/\mathcal{P}_f \to g^{-1}$. Qualitatively similar behavior was observed in the high-speed AFM experiments (20), where the TH rarely detached without resulting in a forward step. On the other hand, essentially every time the LH detaches, it will rebind to its original location (L stomp) because the power stroke constraint prevents it from reaching the backward site. For example, in the $F = 0$ slice of Fig. 1*D*, $\mathcal{P}_f \approx g/(1+g) = 0.89$ and $\mathcal{P}_{Ls} \approx 1/(1+g) = 0.11$. The other pathways do not contribute significantly.

Binding Dynamics and the Average Step Trajectory at Zero Load. The mean times t_{Tb} and t_{Lb} for the TH and LH to bind after detachment (irrespective of the binding site) are related to $t_{fp}^{\pm}$ as

$$t_{Tb} = t_h + \frac{t_{fp}^{+}}{1+b\alpha}, \qquad t_{Lb} = \frac{t_{fp}^{+}}{b+\alpha}. \qquad [5]$$

These binding times are plotted in Fig. 2 *A* (*Upper*) and *B* (*Upper*) as a function of l_p and ν_c. The detached TH has to undergo hydrolysis before rebinding, so $t_{Tb} > t_h$. For the parameters in Table 1, $t_{fp}^{+} = 0.3$ ms and $t_h = 1.3$ ms at $F = 0$, so hydrolysis is the rate-limiting step for TH binding. As noted above, T foot stomping is infrequent in this case, so the binding events contributing to t_{Tb} are almost exclusively forward steps. We note, *en passant*, that our value for t_{fp}^{+} agrees well with the $F = 0$ result of Brownian dynamics simulations (35), further validating the analytical model for the diffusive search.

A closely related quantity to the mean binding time is the cumulative probability that the head has bound to a particular binding site at time t after detachment. For the TH, the probability $\mathcal{P}_{Tb}^{\pm}(t)$ for the site $\mathbf{r}_{\pm}$ is given by

$$\mathcal{P}_{Tb}^{+}(t) = \frac{t_h\left(1-e^{-t/t_h}\right) - t_{fp}^{+}(1+b\alpha)^{-1}\left(1-e^{-t/t_{fp}^{+}}\right)}{t_h(1+b\alpha) - t_{fp}^{+}},$$
$$\mathcal{P}_{Tb}^{-}(t) = b\alpha \mathcal{P}_{Tb}^{+}. \qquad [6]$$

From $\mathcal{P}_{Tb}^{\pm}(t)$, we can calculate an experimentally measurable quantity, the average distance traveled by the free end along the z axis after detachment, $\langle \delta z(t) \rangle = \langle z(t) - z(0) \rangle$, where $z(0) = -\Delta$. The result is

$$\langle \delta z(t) \rangle = (\mu_z + \Delta)\left(1 - \mathcal{P}_{Tb}^{+}(t) - \mathcal{P}_{Tb}^{-}(t)\right)\left(1 - e^{-t/t_r}\right) + 2\Delta \mathcal{P}_{Tb}^{+}(t). \qquad [7]$$

The first term represents the contribution from the ensemble of trajectories where the TH is still unbound: a fast polymer relaxation over time t_r from the initial point at $z(0) = -\Delta$ to the equilibrium average position μ_z (Eq. **2**). The second term represents the fraction of the ensemble where the TH has successfully bound to the forward site, which eventually corresponds to the entire ensemble for sufficiently large t. Thus, $\delta z(t)$ has two regimes, as shown in Fig. 3: a steep rise to $\mu_z + \Delta$ on time scales $t \lesssim t_r$,

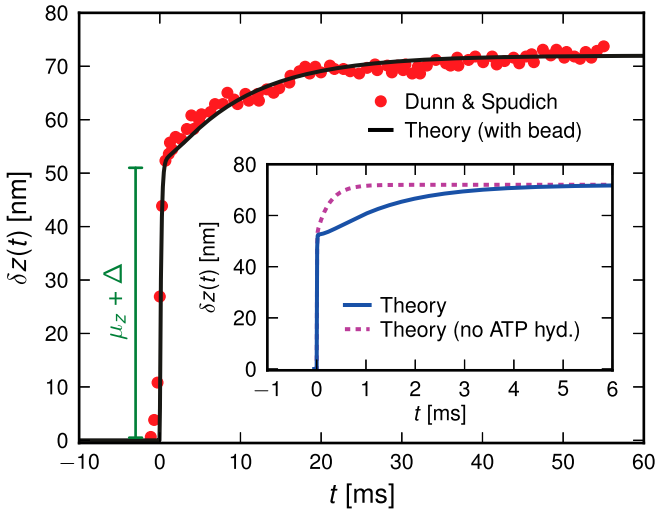

Fig. 3. Mean step trajectory $\langle \delta z(t) \rangle$ of the detached head along the actin filament at zero load. Red dots are the experimental results of Dunn and Spudich (23), obtained by tracking a gold nanoparticle attached near the end of the MyoV lever arm. A fast rise occurs over a distance $\mu_z + \Delta$, resulting from the polymer structure relaxing to equilibrium after TH detachment. The more gradual rise that follows corresponds to the diffusive search for the forward binding site. The solid curve is the theoretical prediction, corrected for the slowing down of relaxation and first passage dynamics due to the particle. (*Inset*) Result of the original theory without the correction (solid curve), compared with a variant of the theory where ATP hydrolysis (hyd.) is removed as a condition for the TH to bind (dashed curve).

followed by a slower ascent to the full step distance 2Δ. Dunn and Spudich (23) have measured $\langle \delta z(t) \rangle$ for MyoV by attaching a 40-nm diameter gold nanoparticle near the end of one lever arm. Observing the particle through dark-field imaging, they aligned and averaged 231 individual step trajectories to produce the $\langle \delta z(t) \rangle$ data points shown in Fig. 3. Because the nanoparticle is sufficiently large that its hydrodynamic drag will slow down the relaxation and diffusive dynamics, we included a time rescaling factor B into the theory to account for the effect of the bead: $t_{\rm fp}^{+} \to B t_{\rm fp}^{+}$, $t_{\rm r} \to B t_{\rm r}$. The theory agrees well with the experiment for $B = 29$ and $\theta_c = 60^{\circ}$. The fitted value of θ_c is based on setting the experimentally measured steep rise, ≈52 nm, equal to $\mu_z + \Delta$, with μ_z given by Eq. **2**. The θ_c value is insensitive to the precise value of ν_c or l_p (assuming we are in the $\nu_c \gg 1$ and $\kappa \ll 1$ regime), as well as to the time rescaling B. In the experiment, the relaxation time for the steep rise was faster than the equipment time resolution of 320 ms. In our theory, the rescaled relaxation time is $B t_{\rm r} \approx 145$ ms, which satisfies this upper bound. After the steep rise, the remaining ascent of ≈20 nm to the full step distance is determined by the diffusive search and binding to the forward site. According to Eqs. **6** and **7**, this part of the step involves two time scales, $t_{\rm h}$ and $t_{\rm fp}^{+}$. Although $t_{\rm fp}^{+} \approx 0.33$ ms is smaller than $t_{\rm h} = 1.3$ ms, the rescaled $B t_{\rm fp}^{+} = 9.7$ ms $> t_{\rm h}$; thus, in this particular case, hydrolysis is not rate-limiting.

However, by changing the ATPase properties of the motor head, one can experimentally observe the role of hydrolysis in the binding kinetics. The nanoparticle tracking results described above are for MyoV with essential light chain LC1sa at the lever arm binding site closest to the motor head and calmodulin along the remainder of the arm. We will denote this type as MyoVelc. Dunn and Spudich (23) also studied a variant with only calmodulin (MyoVcam) that has very different ATPase rates. As shown in an earlier bulk study (43), for MyoVelc, the reverse $t_{-\rm h}^{-1}$ is negligible compared with the forward rate ($t_{\rm h}^{-1} = 750$ s^{-1} from Table 1) with $t_{\rm h}/t_{-\rm h} < 0.1$. In contrast, for MyoVcam, the forward rate is more than fourfold slower, $t_{\rm h}^{-1} = 162$ s^{-1}, and the reverse rate is substantial, $t_{-\rm h}^{-1} = 216$ s^{-1} (43). With nonnegligible $t_{-\rm h}^{-1}$ and the bead rescaling factor B, Eq. **5**. for the TH binding time becomes

$$t_{\rm Tb} = t_{\rm h} + \frac{B t_{\rm fp}^{+}}{1 + b\alpha}\left(1 + \frac{t_{\rm h}}{t_{-\rm h}}\right). \qquad [8]$$

By substituting the $t_{\rm h}^{-1}$ and $t_{-\rm h}^{-1}$ estimates for MyoVcam from ref. 43, while keeping all other parameters the same, Eq. **8**. predicts a MyoVcam binding rate of $t_{\rm Tb}^{-1} = 35$ s^{-1}, which is about 2.6-fold slower than for MyoVelc, where $t_{\rm Tb}^{-1} = 91$ s^{-1}. Dunn and Spudich estimated the rebinding rates from the nanoparticle trajectories and found a similar threefold decrease between the MyoVelc and MyoVcam systems, from 180 ± 50 s^{-1} down to 60 ± 15 s^{-1} (23). The experimental rebinding rates are faster than the theoretical ones, which may be due, in part, to the fact that, experimentally, rebinding is not directly observed but only approximately inferred from where the $\delta z(t)$ trajectory covers the full distance 2Δ to the forward site. The myosin head could still diffuse near 2Δ for some time without binding, and this could be indistinguishable from a binding event due to the intrinsic noise in the trajectory. However, the general slowdown seen in the experiment is reproduced in the theory and highlights the interplay of hydrolysis and diffusion times in the binding dynamics.

The hydrolysis rate would also play a greater role if the impediment of the attached bead were removed. For the MyoVelc case, with a bead factor $B = 29$, the free end has enough time to hydrolyze before finding the forward binding site. Thus, the decay after the steep rise is mainly a single exponential in Fig. 3, with a characteristic time $B t_{\rm fp}^{+}$. If a future experiment were to measure $\langle \delta z(t) \rangle$ without slowing down the diffusion, we should see the average step shape shown in Fig. 3 (*Inset*), predicted by the theory for $B = 1$. There is a more gradual, double-exponential decay after the steep rise, reflecting both the $t_{\rm h}$ and $t_{\rm fp}^{+}$ time scales. For comparison, we also show the results of the theory without ATP hydrolysis as a precondition for binding so as to emphasize the change in the $\langle \delta z(t) \rangle$ shape due to $t_{\rm h}$.

Experimentally, one can also study the average z-axis trajectory of the center of mass, for example, in a single-molecule bead assay (19). The results are essentially similar, but the above-cited distances are halved: We have a fast rise of ≈26 nm corresponding to the power stroke, detachment, and polymer relaxation, and a remaining slow ascent of ≈10 nm due to diffusive search and binding, giving a combined 36-nm center-of-mass step.

Run Length at Zero Load. The final observable quantity of interest at $F = 0$ is the mean run length along the actin filament. Assuming $t_{\rm d1} \gg t_{\rm Lb}, t_{\rm Tb}$, the average run length $z_{\rm run}$ at any F is given by

$$z_{\rm run} = v_{\rm run} t_{\rm run}, \quad v_{\rm run} \approx \frac{\Delta}{t_{\rm d1}}\left(\frac{1}{1 + b\alpha} - \frac{\alpha}{g(b + \alpha)}\right), \quad t_{\rm run} \approx \frac{g t_{\rm d1}^{2}}{t_{\rm Lb} + g t_{\rm Tb}}, \qquad [9]$$

where $v_{\rm run}$ and $t_{\rm run}$ are the mean run velocity and duration, respectively. The positive and negative terms in $v_{\rm run}$ are contributions from forward and backward stepping, respectively. Experimental estimates for $z_{\rm run}$ at $F = 0$, plotted on the left edge of Fig. 4*B*, vary over a wide range from 0.7 – 2.4 μm (6, 10, 11), most likely due to different measurement conditions (particularly the KCl concentration of the buffer). We choose as a representative value $z_{\rm run} = 1.3$ μm, which allows us to use Eq. **9** at $F = 0$ to solve for the binding penalty parameter, $b = 0.065$. This can be done because $\alpha \ll 1$ at zero load, and substituting $\alpha = 0$ in Eq. **9** leads to an expression that is roughly independent of ν_c for large ν_c. Thus, we have fit two of the free parameters, θ_c and b, by comparison with experimental values for the rise $\mu_z + \Delta$ and the run length $z_{\rm run}$, respectively. The final free parameter, ν_c, will be fit by comparison with the stall force, which is discussed in the next section.

Load Dependence of the Kinetic Pathways and a Simple Formula for Stall Force. When a backward force is applied to MyoV, it counteracts the bias due to the power stroke constraint, bending the bound leg and shifting the equilibrium away from the forward binding site. We see this directly in Eq. **3** for α, where the $\beta \Delta F \cos\theta_F$ term in the exponential has the opposite sign of the $-\Delta \mathcal{T} L^{-1} \cos\theta_c$ contribution from the constraint. Thus, α increases rapidly with increasing F, eventually becoming greater than 1, meaning that reaching the backward site is faster than reaching the forward one. Fig. 2*C* plots $t_{\rm fp}^{\pm}$ and the leg binding times as a function of F for the parameter set in Table 1. The changeover from $\alpha < 1$ to $\alpha > 1$ occurs near $F = 1.4$ pN. The corresponding pathway probabilities are in Fig. 1*D*. With increasing force, each leg changes its primary kinetic pathway. TH detachment, which almost always leads to forward stepping at small F, instead leads to T foot stomping at high F. Similarly, LH detachment results in mainly L foot stomps at low F but leads to backward stepping at high F. Thus, application of a resistive load totally alters the partitioning between the kinetic pathways.

At the stall force, $F_{\rm stall}$, the probabilities of backward and forward stepping are equal, and the mean MyoV velocity goes to zero. Setting $\mathcal{P}_{\rm b}/\mathcal{P}_{\rm f}$ from Eq. **4** equal to 1, substituting α from Eq. **3**, we obtain

$$F_{\text{stall}} = \frac{\mathcal{T}\cos\theta_c}{\beta L\cos\theta_F} + \frac{1}{\beta\Delta\cos\theta_F}\log\frac{g-1+\sqrt{(g-1)^2+4gb^2}}{2b} \quad [10]$$
$$\equiv F^{\text{p}}_{\text{stall}} + F^{\text{c}}_{\text{stall}},$$

where the power stroke effectiveness $\mathcal{T}$ is defined in Eq. **3** in terms of l_p, L, and ν_c. The stall force has two main contributions. The first term $F^{\text{p}}_{\text{stall}}$ is due to the power stroke constraint, depending on $\mathcal{T}$ and θ_c, and thus the structural parameters that determine $\mathcal{T}$. Larger $\mathcal{T}$ and smaller θ_c both act to shift the free end probability distribution closer to the forward site, impeding back-stepping and contributing to a larger F_{stall}. The second term $F^{\text{c}}_{\text{stall}}$ arises from two properties of MyoV head chemistry: the gating ratio g that controls how often the TH detaches relative to the LH and the binding penalty due to incorrect head orientation near the binding site. Increasing g makes detachment of the LH less common. Because back-stepping requires LH detachment, it will also become less probable. The importance of b is related to the Pr orientation penalty, which makes binding to the backward site less favorable. Larger g or smaller b reduces $\mathcal{P}_b/\mathcal{P}_f$ at any given F, thus increasing F_{stall}. If there were no gating asymmetry (the ratio $g = 1$), then the contribution $F^{\text{c}}_{\text{stall}}$ vanishes.

The optical trap experiment of Kad et al. (16) yielded $\mathcal{P}_b/\mathcal{P}_f$ as a function of F. The data are plotted in Fig. 4*A*, corresponding to an estimated $F_{\text{stall}} \approx 1.9$ pN. Using this experimental value of F_{stall} and assuming, for simplicity, that $\theta_F = 0$ or a pure backward load, we get $\nu_c = 184$ by solving Eq. **10**. In *Discussion*, we will return to the magnitude of ν_c in the broader context of stiffness and energetics within the myosin motor family. The theoretical curve in Fig. 4*A* is in good agreement with the experimental data points over the entire measured F range. Back-stepping is mostly suppressed for $F \lesssim 1$ pN, and then rapidly increases until the stall point.

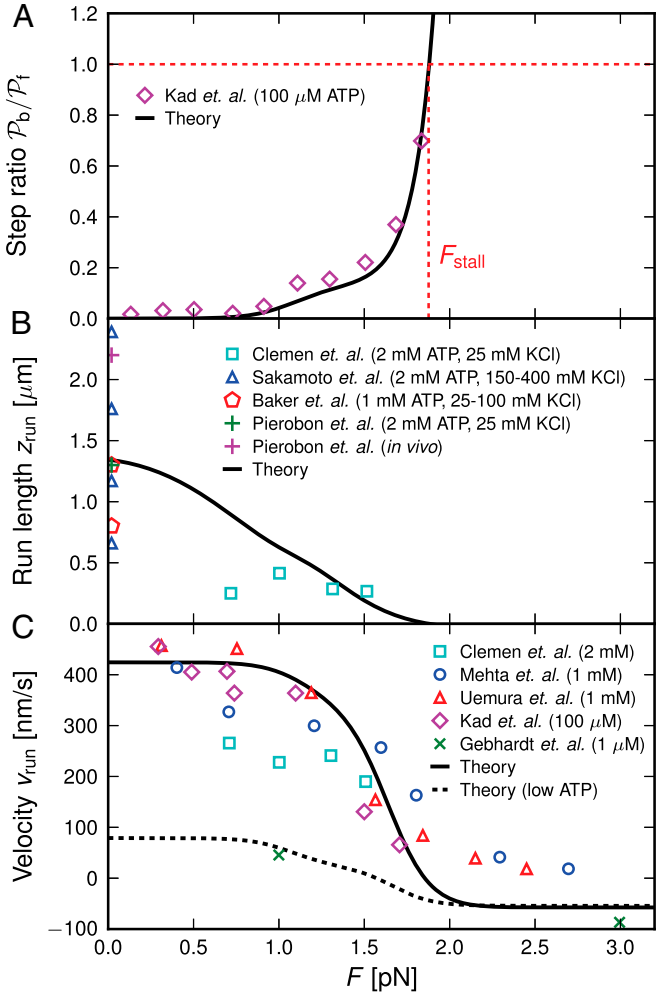

Fig. 4. Comparison of the theory predictions (solid curves, with parameters in Table 1) to experimental results (symbols) as a function of load force F (with $\theta_F = 0$). For the legends, the first and second terms in the parentheses correspond to experimental ATP and KCl concentrations, respectively. Where the KCl concentration is not indicated, the value is 25 mM. (*A*) Ratio of backward to forward steps, $\mathcal{P}_b/\mathcal{P}_f$, compared with the data of Kad et al. (16). (*B*) Run length, z_{run}, compared with the data of Sakamoto et al. (6), Baker et al. (10), Pierobon et al. (11), and Clemen et al. (36). (*C*) Velocity, v_{run}, compared with the data of Mehta et al. (4), Kad et al. (16), Uemura et al. (17), Gebhardt et al. (18), and Clemen et al. (36). The dashed curve corresponds to a modified version of the theory, which accounts for the low ATP concentration in the experiment of Gebhardt et al. (18) (main text).

Run Length and Velocity Under Load. The change in kinetic pathways with F manifests itself in two other observables, the mean run length z_{run} and velocity v_{run}, which both decrease to zero as the stall force is approached. In Fig. 4 *B* and *C*, we show various experimental results for these two quantities as a function of F, together with the theoretical prediction (Eq. **9**). Aside from one exception mentioned below, all the experiments were done at saturating ATP ($\gtrsim 100$ μM). Despite the scatter in the experimental values, the theory reproduces the overall trends well. The motor function nears its unloaded ($F = 0$) velocity of $v_{\text{run}} = 414$ nm/s ($\approx \Delta t_{d1}^{-1}$) for small forces and then slows down noticeably for $F \gtrsim 1$ pN as the proportion of back steps increases. The extrapolated force at which the velocity goes to zero is another way to estimate the stall force, and the experiments show MyoV stalling in the range of $F \approx 1.9-3$ pN.

Above the stall force, the theory predicts a small net negative velocity, because back steps outnumber the forward steps. Although the present theory will likely require modifications at very high forces far into the superstall regime, we can tentatively compare our results with those of Gebhardt et al. (18) at $F = 1$ pN and $F = 3$ pN (green crosses in Fig. 4*C*), where the latter data point was just above stall and exhibited a small negative velocity ≈ -90 nm/s. In this case, the ATP concentration is 1 μM, which makes ATP binding the rate-limiting step in TH detachment. To accommodate this, we set $t_{d1}^{-1} = 2.2$ s^{-1}, which is the binding rate at 1 μM ATP estimated from the experimental kinetics (18). With this single modification, the theory gives the dashed curve in Fig. 4*C*, which roughly captures the velocities both below and above stall. Taken together, the comparison between the theory and a number of experimental results shows that our predictions agree with measurements remarkably well.

Discussion

Constraints on MyoV Structural and Binding Parameters. MyoV walks nearly unidirectionally at zero load and can persist against backward loads up to the stall force. Is the system robust to variations in the parameter space? To make the question concrete, we can ask under what conditions does MyoV fulfill two requirements for processive motion and the ability to sustain load: (*i*) the backward-to-forward step ratio at zero load, $\mathcal{P}_b/\mathcal{P}_f \le \epsilon$, and (*ii*) the stall force F_{stall} falls in some range from $F^{\text{min}}_{\text{stall}}$ to $F^{\text{max}}_{\text{stall}}$ when the resistive load is applied parallel to the actin axis ($\theta_F = 0$ in Fig. 1*B*). We choose experimentally motivated values of $\epsilon = 0.01$, $F^{\text{min}}_{\text{stall}} = 1.9$ pN (16), and $F^{\text{max}}_{\text{stall}} = 3.0$ pN (4, 12, 17). From Eqs. **3**, **4**, and **10**, these two conditions are satisfied within the blue-shaded area of Fig. 5*A*, which plots a $\log b$ vs. $\mathcal{T}$ slice of the parameter space, with fixed θ_c, Δ, and g. Along the $\mathcal{T}$ axis, the region has minimal and maximal boundaries:

$$\mathcal{T}_{\min} = \frac{L}{2\Delta\cos\theta_c}\left(\beta\Delta F_{\text{stall}}^{\min} + \log\frac{(1-\epsilon g)e^{\beta\Delta F_{\text{stall}}^{\min}} - 1 + g}{g\left(\epsilon(g-1)e^{\beta\Delta F_{\text{stall}}^{\min}} + 1 - \epsilon g\right)}\right) = 16.6,$$

$$\mathcal{T}_{\max} = \frac{L}{\Delta\cos\theta_c}\left(\beta\Delta F_{\text{stall}}^{\max} - \log g\right) = 47.0,$$

[11]

where the numerical values are computed for the specific parameters in Table 1. If $\mathcal{T} < \mathcal{T}_{\min}$ or $\mathcal{T} > \mathcal{T}_{\max}$, there is no value of b where conditions *i* and *ii* are satisfied simultaneously. A density plot of $\mathcal{T}$ in terms of ν_c and l_p is shown in Fig. 5*B*, with the $\mathcal{T}_{\min} \le \mathcal{T} \le \mathcal{T}_{\max}$ region shaded in green. Asymptotically, this region is bounded by a minimum persistence length $l_p^{\min}$ for $\nu_c \to \infty$ and minimum constraint strength $\nu_c^{\min}$ for $l_p \to \infty$:

$$l_p^{\min} = \frac{7L}{20}(\mathcal{T}_{\min} - 1) = 192 \text{ nm}, \qquad \nu_c^{\min} = \mathcal{T}_{\min} - 1 = 15.6.$$

[12]

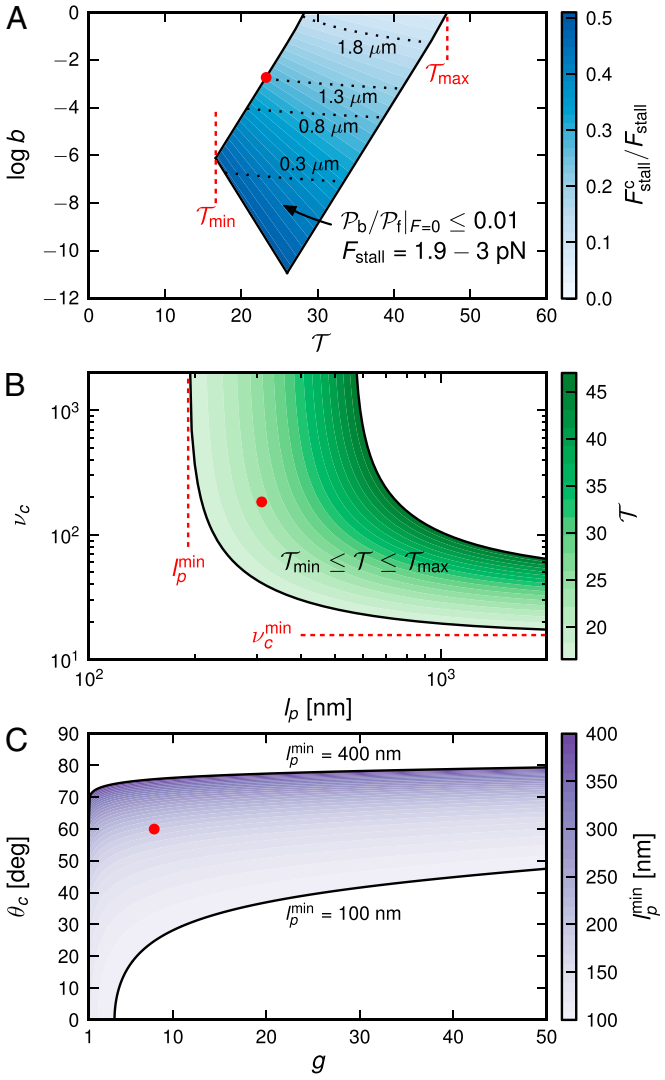

Fig. 5. Exploring the design space for MyoV satisfying the constraints that $\mathcal{P}_b/\mathcal{P}_f < 0.01$ and that the stall force F_{stall} be in the range of 1.9 – 3 pN. The red dot in each panel corresponds to the parameter set in Table 1. (*A*) Blue-shaded region shows the allowed values for the binding penalty b and power stroke effectiveness $\mathcal{T}$ (Eq. **3**). The intensity of the shading indicates the fraction $F_{\text{stall}}^c/F_{\text{stall}}$, where F_{stall}^c is the contribution of head chemistry to the total stall force (Eq. **10**). The labeled black dotted lines correspond to loci of constant run length z_{run}. The blue-shaded region falls entirely within the range of $\mathcal{T}_{\min} = 16.6$ to $\mathcal{T}_{\max} = 47.0$ along the $\mathcal{T}$ axis. (*B*) Green-shaded region corresponds to those values of persistence length l_p and power stroke strength ν_c that yield $\mathcal{T}$ in the range of $\mathcal{T}_{\min}$ to $\mathcal{T}_{\max}$. The intensity of shading indicates the magnitude of $\mathcal{T}$. Below the values $l_p^{\min} = 192$ nm and $\nu_c^{\min} = 15.6$, it is impossible to satisfy the bounds on $\mathcal{T}$. (*C*) Purple-shaded region corresponds to values of the gating ratio g and power stroke constraint angle θ_c that yield $l_p^{\min}$ from 100 – 400 nm, with the shading intensity proportional to $l_p^{\min}$.

Having l_p and ν_c above these two minima constitutes necessary but not sufficient conditions for $\mathcal{T}$ to fall between $\mathcal{T}_{\min}$ and $\mathcal{T}_{\max}$. Physically, $\mathcal{T}$ represents the effectiveness of the power stroke constraint, which is directly related to l_p and ν_c through Eq. **3**. We thus see that motor function with the given specifications requires a certain minimal power stroke effectiveness, which cannot be achieved unless both the persistence length of the lever arms and the strength of the end-tangent constraint are large enough. If either l_p or ν_c is too small, back-stepping becomes more frequent at zero load and it is easier to bend the bound leg backward, resulting in stall being reached at smaller force magnitudes.

The bounds on $\mathcal{T}$ in Eq. **11** also depend on the gating ratio g and Po orientation θ_c (Fig. 1*B*), which we illustrate in Fig. 5*C* by plotting the density of $l_p^{\min}$ (related to $\mathcal{T}_{\min}$ through Eq. **12**) in terms of g and θ_c. By showing only the range $l_p^{\min} = 100 - 400$ nm, comparable with estimates of the lever arm persistence length (26, 28), we see there are constraints on the angle θ_c that vary depending on g. Angles too close to 90° give insufficient forward bias and have to be compensated for by an unrealistically stiff lever arm $l_p^{\min} > 400$ nm. As θ_c decreases, $l_p^{\min}$ decreases, because the stronger forward bias means that one can use progressively more flexible lever arms and still get efficient motility and resistance to load.

The parameter range where the motility conditions *i* and *ii* are simultaneously satisfied (the shaded region in Fig. 5*A*), is broad, encompassing a wide swathe of possible b values. To restrict the parameters further, we can specify that MyoV exhibit a certain run length. The dotted lines in Fig. 5*A* are loci of constant z_{run}, with the red dot marking the parameter set in Table 1 (where $z_{\text{run}} = 1.3$ μm and $F_{\text{stall}} = 1.9$ pN). Even with this restriction, we still have a range of possible $\mathcal{T}$ values at each z_{run}, which corresponds to a region in the space of l_p and ν_c. Interestingly, the system has a degree of robustness against changes in the structural parameters and can meet the basic requirements for function with a high-duty ratio assuming l_p and ν_c yield a $\mathcal{T}$ within the allowed range.

Relative Contributions of Power Stroke and Head Chemistry to the Stall Force Magnitude. Although the emphasis in the preceding section has been on the structural parameters, it is important to note the complementary role of head chemistry (determined by the nucleotide state of MyoV) in producing the observed stall force. If TH and LH detachment were equally probable ($g = 1$), the F_{stall}^c term in Eq. **10** would be zero, and $F_{\text{stall}} = F_{\text{stall}}^p$. From the definition of α in Eq. **3**, one can see that F_{stall}^p is the force magnitude at which $\alpha = 1$. In other words, at $g = 1$, the only condition for stall is that the first passage times to the forward and backward sites are equal. In fact, the value of F_{stall}^p arises from a simple force balance: Stall occurs when the component $F\cos\theta_F$ of the backward load along the z axis equals $(\mathcal{T}/\beta L)\cos\theta_c$, the z component of an effective forward force $(\mathcal{T}/\beta L)$ oriented along the power stroke constraint direction. This is another way of interpreting the power stroke parameter $\mathcal{T}$, relating it to a counteracting force on the joint to oppose the load. When the two forces are equal, there is no bias either forward or backward and $\alpha = 1$.

Head chemistry changes the picture, by making LH detachment less frequent ($g > 1$) and introducing a binding penalty ($b < 1$) for the wrong head orientation at the binding site. A small b parameter reduces the probability of T foot stomping, which

would otherwise compete more easily with forward stepping at large loads and reduce the likelihood of the latter. This is the beneficial role of the recovery stroke highlighted in the study by Shiroguchi et al. (3). The outcome is an additional contribution F^{c}_{stall} to F_{stall}, which means stall is delayed until we reach a value of $\alpha > 1$. In order for back-stepping to be as likely as forward stepping, it is not enough to make the first passage times to the two binding sites equal. We have to make t^{-}_{fp} fast enough compared with t^{+}_{fp} to compensate for the gating and binding biases. To illustrate the significance of the F^{c}_{stall} contribution over the allowed parameter range, we use the intensity of the shading in Fig. 5*A* to represent $F^{c}_{\text{stall}}/F_{\text{stall}}$, the fraction of the stall force magnitude due to the head chemistry term. The fraction values vary from $\approx 0.08 - 0.49$, with the parameter set in Table 1 giving $F^{c}_{\text{stall}}/F_{\text{stall}} = 0.28$. Although the power stroke term always dominates, head chemistry has a smaller but nonnegligible role in helping MyoV move forward under load.

Relation of the Power Stroke Constraint Strength to Myosin Stiffness and Thermodynamic Efficiency. The mechanical compliance of MyoV under load is determined both by the bending stiffness of the lever arm l_p and the strength of the effective end-tangent constraint ν_c. The latter arises at a molecular level from the bending stiffness of the flexible joint between the motor head and lever arm domains. If we suppose this joint involves subdomains (i.e., the converter region of the motor head) on length scales of ~ 1 nm, then $\nu_c = 184$ corresponds to a persistence length of ~ 184 nm for the head–arm joint, which is reasonable because it is of the same order of magnitude as the persistence length, $l_p = 310$ nm, of the lever arm itself.

The complex coupling between these two different bending rigidities is reflected in the power stroke effectiveness parameter $\mathcal{T}$, which depends nonlinearly on both l_p and ν_c. In fact, one can approximately relate $\mathcal{T}$ to the overall compliance of the head–arm system. For large l_p, where the arms are nearly rigid rods, the backward force ($\theta_F = 0$) required to keep the end of the bound leg at an angle $\theta_c' > \theta_c$ (*Materials and Methods*) is

$$F \approx \frac{\mathcal{T}}{\beta L} \frac{\sin(\theta_c' - \theta_c)}{\sin \theta_c'}. \qquad [13]$$

The horizontal δz displacement corresponding to the angular displacement between θ_c' and θ_c is $\delta z \approx L(\cos\theta_c - \cos\theta_c')$. For $\theta_c' = 60° - 120°$, the rough angular range during the motor cycle, F scales almost linearly with δz, with a slope $k \approx \mathcal{T}/\beta L^2$ that gives an effective total spring constant of the bound leg. In the strained telemark stance of the waiting state, when both legs are bound and Po, and the L leg is bent backward from $\theta_c = 60°$ to about $\theta_c' = 120°$, $\delta z \approx L$ and the effective spring is loaded with a mechanical energy of $E_{\text{wait}} = k\delta z^2/2 = \mathcal{T}/2\beta$. This is essentially the energy necessary for the power stroke (Pr to Po) transition that loads the spring. For $l_p = 310$ nm and $\nu_c = 184$, we have $\mathcal{T} = 23.2$, $k = 0.078$ pN/nm, and $E_{\text{wait}} = 11.6\, k_B T$. If the total energy available from ATP hydrolysis is $\approx 24\, k_B T$, then this corresponds to a thermodynamic efficiency of nearly 50%, similar to earlier estimates for MyoV (30) and myosin II (44). The tension in the waiting state associated with this stored mechanical energy is $F_{\text{wait}} = k\delta z = 2.7$ pN.

Myosin II offers an interesting point of comparison in terms of mechanical compliance. The stiffness k of its S1 domain is a key parameter in the swinging cross-bridge model of muscle contraction, with a range of $k \approx 1 - 3$ pN/nm inferred from experimental measurements (26, 45, 46), which is an order of magnitude higher than our MyoV value above. The key factor underlying this difference is the length of the lever arm, with myosin II having an L about one-third that of MyoV. If one assumes that beyond this difference, the other structural factors (l_p and ν_c) are similar between these two systems, then one can use our structural model with $l_p = 310$ nm, $\nu_c = 184$, and $L = 12$ nm to predict a myosin II stiffness of $k = 1.5$ pN/nm, which compares well with the experimental range.

Conclusion

In conclusion, we have proposed a model of MyoV dynamics based on the polymeric nature of the lever arms and the probability distribution of their fluctuations during the diffusive search for actin-binding sites. Using only three experimentally unknown parameters, our theory quantitatively captures many experimental outcomes, such as the time dependence of the mean trajectory of the detached head and the force dependence of the probability ratio of forward to backward stepping. The theory, which allows us to explore the robustness of stepping to variations in the design of MyoV, also yields testable predictions for novel quantities, like the probabilities of foot stomping as a function of load. Although the unidirectionality of the motor and the stall force magnitude exhibit tolerance to variation in the structural parameters, the theory reveals constraints on the persistence length of the lever arms and power stroke bias. In the context of processive motors within the myosin superfamily, MyoV has the simplest lever arm structure, which can be approximated well by a stiff polymer. Myosins VI and X have evolved qualitatively different lever arms consisting of both stiff and flexible segments (47). The underlying theoretical ideas in our description of MyoV are quite general, and it will be interesting to extend them in the future to more complex geometries. How do the structural constraints change in a motor with heterogeneous persistence length, and can such an approach help resolve the competing hypotheses for the conformation of the myosin VI lever arm (48–50)?

From a broader perspective, the approach we have developed is also applicable in other motor systems, such as dynein and kinesin, provided the structural elements generating the power stroke can be modeled as suitable polymer chains. In addition, there are potential applications to other biological systems that transmit or generate force, such as microtubules and cytoskeletal structures.

Materials and Methods

First Passage Times to Binding Sites. The derivation of Eq. **1** for the mean first passage times $t^{\pm}_{\text{fp}}$ is shown in detail in *SI Text*. The underlying approach is based on the renewal method for first passage problems (51); in the polymer context, this is equivalent to the Wilemski–Fixman theory for diffusion-controlled reactions (52). For analytical tractability, we ignore excluded volume interactions, which would likely lead to a small decrease in the first passage times but would not change the overall order of magnitude. Strictly speaking, $t^{\pm}_{\text{fp}}$ depends on the initial configuration of the polymer, but for MyoV dynamics, $t^{\pm}_{\text{fp}} \gg t_r$, the relaxation time of the polymer to equilibrium. Hence, the memory of the initial configuration is lost during the diffusive search, and the expression for $t^{\pm}_{\text{fp}}$ in Eq. **1** is valid assuming we do not start with the free end in the immediate vicinity of the target. When the latter condition is violated, for example, after failed binding attempts due to wrong head orientation or immediately following detachment from the actin, we assume fast relaxation to equilibrium before the head has a chance to rebind.

Mean Field Theory for Probability Distribution of MyoV Free End During Diffusive Search. The key physical quantity in Eq. **1** that determines the average first passage time to a binding site is $\mathcal{P}(\mathbf{r}_{\pm})$, the equilibrium probability density of finding the detached end of MyoV at $\mathbf{r}_{\pm} = \pm\Delta\hat{\mathbf{z}}$. For a structure of two semiflexible polymer legs, with one leg bound at the origin, the free end-point vector is $\mathbf{r} = \mathbf{r}_f + \mathbf{r}_b$, where $\mathbf{r}_{f/b}$ is the end-to-end vector of the free/bound leg. The distribution $\mathcal{P}(\mathbf{r})$ is a convolution of the individual leg distributions $\mathcal{P}_{f/b}(\mathbf{r}_{f/b})$:

$$\mathcal{P}(\mathbf{r}) = \int d\mathbf{r}_b \int d\mathbf{r}_f\, \mathcal{P}_b(\mathbf{r}_b)\mathcal{P}_f(\mathbf{r}_f)\delta(\mathbf{r} - \mathbf{r}_b - \mathbf{r}_f). \qquad [14]$$

There is no exact closed form expression for the end-to-end distribution of a semiflexible polymer, although moments of the distribution can be calculated analytically (53, 54). For the free leg, which is not under tension, an earlier mean field theory (55) gives a useful approximation:

$$\mathcal{P}_f(\mathbf{r}_f) = A_f \xi_f^{-9/2} \exp\left(-\frac{3\kappa}{4\xi_f}\right), \qquad [15]$$

where $\kappa = L/l_p$, $\xi_f = 1 - r_f^2/L^2$, and A_f is a normalization constant:

$$A_f = \frac{9\sqrt{3}e^{3\kappa/4}\kappa^{7/2}}{8\pi^{3/2}L^3(3\kappa^2 + 12\kappa + 20)}. \quad [16]$$

As shown in *SI Text*, this mean field approach can be generalized to include the end-tangent constraint and load force in the bound leg case, yielding

$$\mathcal{P}_b(\mathbf{r}_b) = A_b\xi_b^{-9/2}\exp\left(-\frac{3\kappa}{4\xi_b} + \mathcal{T}'\,\hat{\mathbf{u}}_c'\cdot\hat{\mathbf{r}}_b\right), \quad [17]$$

where $\xi_b = 1 - r_b^2/L^2$, $\hat{\mathbf{r}}_b = \mathbf{r}_b/r_b$, $\mathcal{T}' = \sqrt{(\mathcal{T}_x')^2 + (\mathcal{T}_z')^2}$, and

$$\mathcal{T}_x' = \mathcal{T}\sin\theta_c + \beta F\,L\sin\theta_F,\ \ \mathcal{T}_z' = \mathcal{T}\cos\theta_c - \beta F\,L\cos\theta_F. \quad [18]$$

The power stroke effectiveness parameter $\mathcal{T}$ is defined in Eq. **3**. The direction $\hat{\mathbf{u}}_c' = \sin\theta_c'\hat{\mathbf{x}} + \cos\theta_c'\hat{\mathbf{z}}$ with an angle θ_c' from the $\hat{\mathbf{z}}$ axis given by

$$\theta_c' = \theta_c + \tan^{-1}\left(\frac{\beta F\,L\sin(\theta_c + \theta_F)}{\mathcal{T} - \beta F\,L\cos(\theta_c + \theta_F)}\right). \quad [19]$$

In the limit of large l_p, the vector $\hat{\mathbf{u}}_c'$ is approximately the average orientation of the bound leg, reflecting the combined influence of the load force F and the end-tangent constraint ν_c. In the case of a backward force ($\theta_F = 0$), we can invert Eq. **19** to find the force F required, on average, to maintain an orientation $\theta_c' > \theta_c$, as shown in Eq. **13**. In both the free and bound leg cases, the analytical distributions $\mathcal{P}_{f/b}(\mathbf{r}_{f/b})$ have excellent agreement with the exactly known moments. Carrying out the convolution in Eq. **14**, we arrive at a final expression for $\mathcal{P}(\mathbf{r}_\pm)$ in the stiff regime ($l_p \gg L$):

$$\mathcal{P}(\mathbf{r}_\pm) \approx \frac{(3\kappa(7\kappa + 20) + 200)\mathcal{T}'}{1{,}600\pi L^2\,\Delta\sinh\mathcal{T}'} I_0\left(\mathcal{T}_x'\sqrt{1 - (\Delta/2L)^2}\right)e^{\pm\frac{\mathcal{T}_z'\Delta}{2L}}, \quad [20]$$

where $I_0(x)$ is the zeroth-order modified Bessel function of the first kind.

ACKNOWLEDGMENTS. M.H. was a Ruth L. Kirschstein National Research Service postdoctoral fellow, supported by the National Institute of General Medical Sciences (Grant 1 F32 GM 97756-1). D.T. was supported by the National Science Foundation (Grant CHE 09-10433) and National Institutes of Health (Grant GM 089685).

1. Spudich JA, Sivaramakrishnan S (2010) Myosin VI: An innovative motor that challenged the swinging lever arm hypothesis. *Nat Rev Mol Cell Biol* 11(2):128–137.
2. Reck-Peterson SL, Provance DW, Mooseker MS, Mercer JA (2000) Class V myosins. *Biochim Biophys Acta* 1496(1):36–51.
3. Shiroguchi K, et al. (2011) Direct observation of the myosin Va recovery stroke that contributes to unidirectional stepping along actin. *PLoS Biol* 9(4):e1001031.
4. Mehta AD, et al. (1999) Myosin-V is a processive actin-based motor. *Nature* 400(6744): 590–593.
5. Rief M, et al. (2000) Myosin-V stepping kinetics: A molecular model for processivity. *Proc Natl Acad Sci USA* 97(17):9482–9486.
6. Sakamoto T, Amitani I, Yokota E, Ando T (2000) Direct observation of processive movement by individual myosin V molecules. *Biochem Biophys Res Commun* 272(2): 586–590.
7. Yildiz A, et al. (2003) Myosin V walks hand-over-hand: Single fluorophore imaging with 1.5-nm localization. *Science* 300(5628):2061–2065.
8. Forkey JN, Quinlan ME, Shaw MA, Corrie JET, Goldman YE (2003) Three-dimensional structural dynamics of myosin V by single-molecule fluorescence polarization. *Nature* 422(6930):399–404.
9. Sakamoto T, Webb MR, Forgacs E, White HD, Sellers JR (2008) Direct observation of the mechanochemical coupling in myosin Va during processive movement. *Nature* 455(7209):128–132.
10. Baker JE, et al. (2004) Myosin V processivity: Multiple kinetic pathways for head-to-head coordination. *Proc Natl Acad Sci USA* 101(15):5542–5546.
11. Pierobon P, et al. (2009) Velocity, processivity, and individual steps of single myosin V molecules in live cells. *Biophys J* 96(10):4268–4275.
12. Veigel C, Wang F, Bartoo ML, Sellers JR, Molloy JE (2002) The gated gait of the processive molecular motor, myosin V. *Nat Cell Biol* 4(1):59–65.
13. Rosenfeld SS, Sweeney HL (2004) A model of myosin V processivity. *J Biol Chem* 279(38):40100–40111.
14. Veigel C, Schmitz S, Wang F, Sellers JR (2005) Load-dependent kinetics of myosin-V can explain its high processivity. *Nat Cell Biol* 7(9):861–869.
15. Purcell TJ, Sweeney HL, Spudich JA (2005) A force-dependent state controls the coordination of processive myosin V. *Proc Natl Acad Sci USA* 102(39):13873–13878.
16. Kad NM, Trybus KM, Warshaw DM (2008) Load and Pi control flux through the branched kinetic cycle of myosin V. *J Biol Chem* 283(25):17477–17484.
17. Uemura S, Higuchi H, Olivares AO, De La Cruz EM, Ishiwata S (2004) Mechanochemical coupling of two substeps in a single myosin V motor. *Nat Struct Mol Biol* 11(9): 877–883.
18. Gebhardt JCM, Clemen AEM, Jaud J, Rief M (2006) Myosin-V is a mechanical ratchet. *Proc Natl Acad Sci USA* 103(23):8680–8685.
19. Cappello G, et al. (2007) Myosin V stepping mechanism. *Proc Natl Acad Sci USA* 104(39):15328–15333.
20. Kodera N, Yamamoto D, Ishikawa R, Ando T (2010) Video imaging of walking myosin V by high-speed atomic force microscopy. *Nature* 468(7320):72–76.
21. Syed S, Snyder GE, Franzini-Armstrong C, Selvin PR, Goldman YE (2006) Adaptability of myosin V studied by simultaneous detection of position and orientation. *EMBO J* 25(9):1795–1803.
22. Beausang JF, Shroder DY, Nelson PC, Goldman YE (2013) Tilting and wobble of myosin V by high-speed single-molecule polarized fluorescence microscopy. *Biophys J* 104(6): 1263–1273.
23. Dunn AR, Spudich JA (2007) Dynamics of the unbound head during myosin V processive translocation. *Nat Struct Mol Biol* 14(3):246–248.
24. Shiroguchi K, Kinosita K, Jr. (2007) Myosin V walks by lever action and Brownian motion. *Science* 316(5828):1208–1212.
25. Komori Y, Iwane AH, Yanagida T (2007) Myosin-V makes two brownian 90 degrees rotations per 36-nm step. *Nat Struct Mol Biol* 14(10):968–973.
26. Howard J, Spudich JA (1996) Is the lever arm of myosin a molecular elastic element? *Proc Natl Acad Sci USA* 93(9):4462–4464.
27. Moore JR, Krementsova EB, Trybus KM, Warshaw DM (2004) Does the myosin V neck region act as a lever? *J Muscle Res Cell Motil* 25(1):29–35.
28. Vilfan A (2005) Elastic lever-arm model for myosin V. *Biophys J* 88(6):3792–3805.
29. Kolomeisky AB, Fisher ME (2003) A simple kinetic model describes the processivity of myosin-v. *Biophys J* 84(3):1642–1650.
30. Lan GH, Sun SX (2005) Dynamics of myosin-V processivity. *Biophys J* 88(2):999–1008.
31. Skau KI, Hoyle RB, Turner MS (2006) A kinetic model describing the processivity of myosin-V. *Biophys J* 91(7):2475–2489.
32. Tsygankov D, Fisher ME (2007) Mechanoenzymes under superstall and large assisting loads reveal structural features. *Proc Natl Acad Sci USA* 104(49):19321–19326.
33. Xu YZ, Wang ZS (2009) Comprehensive physical mechanism of two-headed biomotor myosin V. *J Chem Phys* 131(24):245104.
34. Bierbaum V, Lipowsky R (2011) Chemomechanical coupling and motor cycles of myosin V. *Biophys J* 100(7):1747–1755.
35. Craig EM, Linke H (2009) Mechanochemical model for myosin V. *Proc Natl Acad Sci USA* 106(43):18261–18266.
36. Clemen AEM, et al. (2005) Force-dependent stepping kinetics of myosin-V. *Biophys J* 88(6):4402–4410.
37. Walker ML, et al. (2000) Two-headed binding of a processive myosin to F-actin. *Nature* 405(6788):804–807.
38. De La Cruz EM, Wells AL, Rosenfeld SS, Ostap EM, Sweeney HL (1999) The kinetic mechanism of myosin V. *Proc Natl Acad Sci USA* 96(24):13726–13731.
39. Sellers JR, Veigel C (2010) Direct observation of the myosin-Va power stroke and its reversal. *Nat Struct Mol Biol* 17(5):590–595.
40. Ortega A, Amorós D, García de la Torre J (2011) Prediction of hydrodynamic and other solution properties of rigid proteins from atomic- and residue-level models. *Biophys J* 101(4):892–898.
41. Coureux PD, Sweeney HL, Houdusse A (2004) Three myosin V structures delineate essential features of chemo-mechanical transduction. *EMBO J* 23(23):4527–4537.
42. Thirumalai D, Ha BY (1998) *Theoretical and Mathematical Methods in Polymer Research*, ed Grosberg AY (Academic, New York), pp 1–35.
43. De La Cruz EM, Wells AL, Sweeney HL, Ostap EM (2000) Actin and light chain isoform dependence of myosin V kinetics. *Biochemistry* 39(46):14196–14202.
44. Barclay CJ (1998) Estimation of cross-bridge stiffness from maximum thermodynamic efficiency. *J Muscle Res Cell Motil* 19(8):855–864.
45. Decostre V, Bianco P, Lombardi V, Piazzesi G (2005) Effect of temperature on the working stroke of muscle myosin. *Proc Natl Acad Sci USA* 102(39):13927–13932.
46. Lewalle A, Steffen W, Stevenson O, Ouyang Z, Sleep J (2008) Single-molecule measurement of the stiffness of the rigor myosin head. *Biophys J* 94(6):2160–2169.
47. Sun YJ, Goldman YE (2011) Lever-arm mechanics of processive myosins. *Biophys J* 101(1):1–11.
48. Spink BJ, Sivaramakrishnan S, Lipfert J, Doniach S, Spudich JA (2008) Long single alpha-helical tail domains bridge the gap between structure and function of myosin VI. *Nat Struct Mol Biol* 15(6):591–597.
49. Mukherjea M, et al. (2009) Myosin VI dimerization triggers an unfolding of a three-helix bundle in order to extend its reach. *Mol Cell* 35(3):305–315.
50. Thirumalai D, Zhang ZC (2010) Myosin VI: How do charged tails exert control? *Structure* 18(11):1393–1394.
51. van Kampen NG (2007) *Stochastic Processes in Physics and Chemistry* (North-Holland, Amsterdam), 3rd ed.
52. Wilemski G, Fixman M (1974) Diffusion-controlled intrachain reactions of polymers. 1. Theory. *J Chem Phys* 60(3):866–877.
53. Kratky O, Porod G (1949) Rontgenuntersuchung geloster fadenmolekule. *Recueil Des Travaux Chimiques Des Pays Bas* 68:1106–1122, Dutch.
54. Saito N, Takahashi W, Yunoki Y (1967) Statistical mechanical theory of stiff chains. *J Phys Soc Jpn* 22:219–226.
55. Hyeon C, Thirumalai D (2006) Kinetics of interior loop formation in semiflexible chains. *J Chem Phys* 124(10):104905.

Supporting Information

Hinczewski et al. 10.1073/pnas.1312393110

SI Text

In *SI Text*, we provide the details of the theory that nearly quantitatively explains the complex kinetic pathways in the stepping dynamics of myosin V (MyoV). Because this SI Text is long, containing technical details of the calculations, we begin with a collection of the most important equations, which were used to make the predictions described in the main text. The subsequent sections describe the details leading to these equations.

1. Summary of Key Equations for MyoV Dynamics

First Passage and Binding.

$$t_{\rm fp}^{\pm}=\frac{1}{4\pi a D_{\rm h}\mathcal{P}(\mathbf{r}_{\pm})},\quad t_{\rm Tb}=t_{\rm h}+\frac{t_{\rm fp}^{+}}{1+b\alpha},\quad t_{\rm Lb}=\frac{t_{\rm fp}^{+}}{b+\alpha},\quad \alpha=t_{\rm fp}^{+}/t_{\rm fp}^{-}$$

[S9, S14, and **S19]**

Kinetic Pathway Probabilities.

$$\mathcal{P}_{\rm f}=\frac{g}{1+g}\frac{t_{\rm d1}^{2}}{(1+b\alpha)(t_{\rm d1}+t_{\rm h})(t_{\rm d1}+t_{\rm Tb}-t_{\rm h})},\quad \mathcal{P}_{\rm Ts}=b\alpha\mathcal{P}_{\rm f}$$

[S15 and **S16]**

$$\mathcal{P}_{\rm Ls}=\frac{1}{1+g}\frac{bt_{\rm d1}}{(b+\alpha)(t_{\rm d1}+t_{\rm Lb})},\quad \mathcal{P}_{\rm b}=b^{-1}\alpha\mathcal{P}_{\rm Ls}\quad \textbf{[S20 and S21]}$$

Average Step Shape.

$$\mathcal{P}_{\rm Tb}^{+}(t)=\frac{t_{\rm h}\left(1-e^{-t/t_{\rm h}}\right)-t_{\rm fp}^{+}(1+b\alpha)^{-1}\left(1-e^{-t(1+b\alpha)/t_{\rm fp}^{+}}\right)}{t_{\rm h}(1+b\alpha)-t_{\rm fp}^{+}},$$

$$\mathcal{P}_{\rm Tb}^{-}(t)=b\alpha\mathcal{P}_{\rm Tb}^{+}(t)$$

[S22 and **S23]**

$$\langle\delta z(t)\rangle=(\mu_z+\Delta)\left(1-\mathcal{P}_{\rm Tb}^{+}(t)-\mathcal{P}_{\rm Tb}^{-}(t)\right)\left(1-e^{-t/t_{\rm r}}\right)+2\Delta\mathcal{P}_{\rm Tb}^{+}(t)$$

[S24]

$$\mu_z=l_p\left(1-e^{-L/l_p}\right)\left(\coth\nu_c-\nu_c^{-1}\right)\cos\theta_c\qquad\textbf{[S25]}$$

Mean Run Length and Velocity.

$$z_{\rm run}=v_{\rm run}t_{\rm run},\quad v_{\rm run}\approx\frac{\Delta}{t_{\rm d1}}\left(\frac{1}{1+b\alpha}-\frac{\alpha}{g(b+\alpha)}\right),\quad t_{\rm run}\approx\frac{gt_{\rm d1}^{2}}{t_{\rm Lb}+gt_{\rm Tb}}$$

[S26–S28]

Equilibrium End-Point Probability Distribution.

$$\mathcal{T}\approx 1+\frac{20\nu_c}{20+7\kappa\nu_c},\quad \mathcal{T}'=\sqrt{(\mathcal{T}_x')^2+(\mathcal{T}_z')^2}\qquad\textbf{[S41 and S44]}$$

$$\mathcal{T}_x'=\mathcal{T}\sin\theta_c+\beta F\,L\sin\theta_F,\quad \mathcal{T}_z'=\mathcal{T}\cos\theta_c-\beta F\,L\cos\theta_F\qquad\textbf{[S44]}$$

$$\mathcal{P}(\mathbf{r}_{\pm})\approx\frac{(3\kappa(7\kappa+20)+200)\mathcal{T}'}{1,600\pi L^{2}\Delta\sinh\mathcal{T}'}I_0\left(\mathcal{T}_x'\sqrt{1-\frac{\Delta^{2}}{4L^{2}}}\right)e^{\pm\frac{\mathcal{T}_z'\Delta}{2L}}\qquad\textbf{[S55]}$$

Stall Force.

$$F_{\rm stall}=\frac{k_BT}{\cos\theta_F}\left(\frac{\mathcal{T}}{L}\cos\theta_c+\frac{1}{\Delta}\log\frac{g-1+\sqrt{(g-1)^2+4gb^2}}{2b}\right)$$

[S59]

2. First Passage Times, Binding Probabilities, and Experimental Observables

Mean First Passage Time to a Target Site. After the detachment of one of the MyoV heads from the polar actin tracks, there are two potential actin target sites where the head could rebind, at positions $\mathbf{r}_{\pm}=\pm\Delta\hat{\mathbf{z}}$ (Fig. 1*B*). The axis $\hat{\mathbf{z}}$ is oriented from the minus to plus end of the actin filament, so we denote $\mathbf{r}_{+}$ and $\mathbf{r}_{-}$ as the forward and backward target sites, respectively. Before dealing with the full complexity of the diffusive search and binding for multiple targets (with binding probabilities dependent on the head chemical state), we solve a simpler problem: What is the mean first passage time for the free end of MyoV to reach a sphere of radius a around one of the target sites, for example, $\mathbf{r}_{+}$? (The derivation below will hold analogously for $\mathbf{r}_{-}$, with the + superscripts and subscripts replaced by −.)

Let $f_{\rm fp}(\mathbf{r},\mathbf{r}';t)$ be the distribution of first passage times for the free end to go from an initial position $\mathbf{r}$ to some final position $\mathbf{r}'$. Using the renewal approach (1), the first passage time distribution can be related to the Green's function $G(\mathbf{r},\mathbf{r}';t)$ describing the probability of diffusing from $\mathbf{r}$ to $\mathbf{r}'$ in time t. Choose a final position on a sphere of radius a around the target site $\mathbf{r}_{+}$, so that $\mathbf{r}'=\mathbf{r}_{+}+a\hat{\mathbf{e}}$, where $\hat{\mathbf{e}}$ is any unit vector. The renewal approach relates $f_{\rm fp}$ and G through the integral equation

$$G(\mathbf{r},\mathbf{r}_{+}+a\hat{\mathbf{e}};t)=\int_0^t dt'\int a^{2}d\hat{\mathbf{e}}'\,f_{\rm fp}(\mathbf{r},\mathbf{r}_{+}+a\hat{\mathbf{e}}';t')\times G(\mathbf{r}_{+}+a\hat{\mathbf{e}}',\mathbf{r}_{+}+a\hat{\mathbf{e}};t-t').\qquad\textbf{[S1]}$$

The physical meaning of the equation above is that the Green's function for going from $\mathbf{r}$ to a particular point $\mathbf{r}_{+}+a\hat{\mathbf{e}}$ on the target sphere consists of paths that make first passage at some point $\mathbf{r}_{+}+a\hat{\mathbf{e}}'$ on the target sphere at time $t'\le t$ and then diffuse from $\mathbf{r}_{+}+a\hat{\mathbf{e}}'$ to $\mathbf{r}_{+}+a\hat{\mathbf{e}}$ in time $t-t'$. Because Eq. **S1** is difficult to solve analytically, we make three simplifications, motivated by the observation that the capture radius a is small compared with all other length scales in the problem: (*i*) we approximately average over all final positions on the target sphere, replacing $\mathbf{r}_{+}+a\hat{\mathbf{e}}$ with $\mathbf{r}_{+}$ on both sides of Eq. **S1**; (*ii*) we assume $f(\mathbf{r},\mathbf{r}_{+}+a\hat{\mathbf{e}}';t')$ does not vary appreciably with $\hat{\mathbf{e}}'$ so that it can be replaced by $f_{\rm fp}^{+}(\mathbf{r};t')/4\pi a^{2}$, where $f_{\rm fp}^{+}(\mathbf{r};t')$ is the first passage time distribution for reaching any point on a target sphere of radius a around $\mathbf{r}_{+}$, starting from $\mathbf{r}$; and (*iii*) the Green's function on the right-hand side of Eq. **S1** will not depend significantly on the specific unit vector $\hat{\mathbf{e}}'$ defining the starting position, so we replace $\hat{\mathbf{e}}'$ in the argument of the Green's function by a fixed unit vector $\hat{\mathbf{z}}$. With these approximations, Eq. **S1** becomes

$$G(\mathbf{r},\mathbf{r}_{+};t)\approx\int_0^t dt'\;f_{\rm fp}^{+}(\mathbf{r};t')G\left(\mathbf{r}_{+}+a\hat{\mathbf{z}},\mathbf{r}_{+};t-t'\right).\qquad\textbf{[S2]}$$

The above renewal equation can be solved by Laplace-transforming both sides to yield

$$\tilde{f}^{+}_{\mathrm{fp}}(\mathbf{r};s) \approx \frac{\tilde{G}(\mathbf{r},\mathbf{r}_{+};s)}{\tilde{G}\left(\mathbf{r}_{+}+a\hat{\mathbf{z}},\mathbf{r}_{+};s\right)}, \qquad \text{[S3]}$$

where $\tilde{f}^{+}_{\mathrm{fp}}$ and $\tilde{G}$ are Laplace-transformed functions. For example, $\tilde{G}(\mathbf{r},\mathbf{r}';s) = \int_0^\infty dt\, e^{-st} G(\mathbf{r},\mathbf{r}';t)$, and a similar equation holds for $\tilde{f}^{+}_{\mathrm{fp}}$. The derivative of $\tilde{f}$ with respect to s at $s=0$ is related to the mean first-passage time $t^{+}_{\mathrm{fp}}(\mathbf{r})$ to arrive at the target sphere of radius a around $\mathbf{r}_{+}$:

$$-\frac{\partial}{\partial s}\tilde{f}^{+}_{\mathrm{fp}}(\mathbf{r};s)\Big|_{s=0} = \int_0^\infty dt\, t\, f^{+}_{\mathrm{fp}}(\mathbf{r};t) = t^{+}_{\mathrm{fp}}(\mathbf{r}). \qquad \text{[S4]}$$

We can simplify Eq. **S3** by taking advantage of time scale separation in the system. For $t \gg t_{\mathrm{r}}$, the relaxation time of the two-legged polymer, the Green's function for going from an initial to a final position approaches the equilibrium probability distribution of finding the free end at the final position, $G(\mathbf{r},\mathbf{r}';t) \to \mathcal{P}(\mathbf{r}')$ as $t \to \infty$. In Laplace space, this implies that the Green's function can be decomposed into two contributions:

$$\begin{aligned}\tilde{G}(\mathbf{r},\mathbf{r}';s) &\approx \int_0^{t_{\mathrm{r}}} dt\, e^{-st} G(\mathbf{r},\mathbf{r}';t) + \left(s^{-1}-t_{\mathrm{r}}\right)\mathcal{P}(\mathbf{r}') \\ &\equiv \tilde{G}_0(\mathbf{r},\mathbf{r}';s) + \left(s^{-1}-t_{\mathrm{r}}\right)\mathcal{P}(\mathbf{r}').\end{aligned} \qquad \text{[S5]}$$

For $\tilde{G}(\mathbf{r},\mathbf{r}_{+};s)$ in the numerator of Eq. **S3**, we assume the initial $\mathbf{r}$ is not in the immediate vicinity of the target $\mathbf{r}_{+}$ (which is generally the case for a MyoV diffusive search), so the time to reach the target will be much larger than the relaxation time t_{r}. Hence, $\tilde{G}_0(\mathbf{r},\mathbf{r}_{+};s)$ will be negligible, because $G(\mathbf{r},\mathbf{r}_{+};t)$ is near zero on the time scale $t < t_{\mathrm{r}}$. Thus, we can approximate the numerator of Eq. **S3** as

$$\tilde{G}(\mathbf{r},\mathbf{r}_{+};s) \approx \left(s^{-1}-t_{\mathrm{r}}\right)\mathcal{P}(\mathbf{r}_{+}). \qquad \text{[S6]}$$

For the denominator of Eq. **S3**, $\tilde{G}(\mathbf{r}_{+}+a\hat{\mathbf{z}},\mathbf{r}_{+};s)$, the situation is more complicated, because the initial and final positions are separated by a small distance a; hence, there will be contributions to $\tilde{G}_0$ at short times. In the limit $a \to 0$, the paths between $\mathbf{r}_{+}+a\hat{\mathbf{z}}$ and $\mathbf{r}_{+}$ involve only a fast microscopic rearrangement of the free end, without significant configurational changes in the rest of the structure. If we model the free end as a particle with diffusion constant D, the Green's function in the short time limit can be approximated as (1)

$$G\left(\mathbf{r}_{+}+a\hat{\mathbf{z}},\mathbf{r}_{+};t\right) \approx (4\pi D t)^{-3/2}\exp\left(-a^2/(4Dt)\right). \qquad \text{[S7]}$$

Substituting Eq. **S7** into the integral for $\tilde{G}_0$, we get an expression for the denominator:

$$\begin{aligned}\tilde{G}\left(\mathbf{r}_{+}+a\hat{\mathbf{z}},\mathbf{r}_{+};s\right) &\approx \frac{t_{\mathrm{a}}}{4\pi a^3}\,\mathrm{erfc}\left(\frac{1}{2}\sqrt{\frac{t_{\mathrm{a}}}{t_{\mathrm{r}}}}\right) + \left(s^{-1}-t_{\mathrm{r}}\right)\mathcal{P}(\mathbf{r}_{+}) \\ &\approx \frac{t_{\mathrm{a}}}{4\pi a^3} + \left(s^{-1}-t_{\mathrm{r}}\right)\mathcal{P}(\mathbf{r}_{+}),\end{aligned} \qquad \text{[S8]}$$

where $t_{\mathrm{a}} = a^2/D$ is a microscopic time scale describing how long it takes a particle of diffusivity D to move a distance a. The second approximation in Eq. **S8** assumes $t_{\mathrm{a}} \ll t_{\mathrm{r}}$, which is justified by a simple calculation: Let us set $D = D_{\mathrm{h}}$, where $D_{\mathrm{h}} = 5.7\times10^{-7}\mathrm{cm}^2/\mathrm{s}$ is the diffusion constant of the MyoV head, as derived from the Protein Data Bank structure 1W8J (2) using the program HYDROPRO (3). For $a = 1$ nm, the resulting microscopic time scale is $t_{\mathrm{a}} = 18$ ns, which is significantly smaller than the relaxation time $t_{\mathrm{r}} \sim \mathcal{O}(1\ \mu\mathrm{s})$ of the entire structure (estimates of t_{r} are provided in the next subsection).

Using Eqs. **S6** and **S8** in Eq. **S3**, and then evaluating the derivative in Eq. **S4**, we obtain the final approximate expression for the mean first passage time:

$$t^{+}_{\mathrm{fp}} = \frac{1}{4\pi a D_{\mathrm{h}}\mathcal{P}(\mathbf{r}_{+})}. \qquad \text{[S9]}$$

We have dropped the $\mathbf{r}$ dependence in the notation for $t^{+}_{\mathrm{fp}}(\mathbf{r})$, because the first passage time result is independent of the initial position $\mathbf{r}$. This reflects the underlying assumption that the configurational relaxation time $t_{\mathrm{r}} \ll t^{+}_{\mathrm{fp}}$, so the free end loses memory of its initial position during the long diffusive search. An analogous result holds for the mean first passage time t^{-}_{fp} to the backward target site, with $\mathbf{r}_{+}$ replaced by $\mathbf{r}_{-}$ in Eq. **S9**. A result similar in spirit to Eq. **S9** but without the benefit of derivation was conjectured earlier (4).

To validate the approximation underlying Eq. **S7**, we performed Brownian dynamics simulations on a bead-spring semiflexible polymer model of two-legged MyoV (further details are provided in *SI Text*, *Relaxation Times*). By generating many individual trajectories of the detached polymer end point diffusing a small distance a from $\mathbf{r}_{+}$ to some point $\mathbf{r}_{+}+a\hat{\mathbf{e}}$, we numerically reconstruct the corresponding Green's function (Fig. S1). The excellent fit of the assumed form in Eq. **S7** for several values of a to the numerical results justifies the approximation.

Relaxation Times. To estimate the relaxation time t_{r} of the two-legged MyoV structure, we performed Brownian dynamics (5) simulations of a bead-spring semiflexible polymer model. Each leg consists of 17 beads of diameter $d = 2$ nm, with an additional bead at the flexible joint between the legs. The beads are connected through harmonic springs of stiffness $200\ k_B T/\mathrm{nm}^2$, where k_B is Boltzmann's constant, and T is temperature. Each leg has a bending elasticity described by a persistence length $l_p = 50-400$ nm. Initially, the end beads are fixed at the two binding sites. The end tangent of the leading leg (the unit vector oriented between the centers of the first two beads) is subject to a harmonic constraint of strength $k_B T\nu_c$ along $\hat{\mathbf{u}}_c$ (at an angle of $\theta_c = 60°$ from the actin filament), with $\nu_c = 50-180$. The joint between the legs is subject to a backward load force of F. The beads are coupled hydrodynamically through the Rotne–Prager tensor (6), and their positions evolve in time numerically according to the Langevin equation. Each simulation lasts 12 μs, where both end beads are bound during the first 2.4 μs and the trailing leg end bead is allowed to diffuse freely during the remaining time. By averaging a large number of individual simulations (1,000–1,250 runs for each distinct parameter set of l_p and ν_c), we can extract the mean relaxation time t_{r} for the z-axis position of the trailing leg end bead to reach equilibrium after detachment.

Fig. S2 shows the resulting values of t_{r} for $\nu_c = 50$ and $\nu_c = 180$, with A plotting t_{r} as a function of l_p and B plotting t_{r} as a function of backward load force F at $l_p = 310$ nm. In the absence of load, $t_{\mathrm{r}} \approx 5$ μs for both values of ν_c over the entire plotted range of l_p (corresponding to the semiflexible regime $l_p > L$). Because relaxation of MyoV requires a rotational reorientation of a stiff, two-legged structure (with each leg of contour length $L = 35$ nm), we expect that t_{r} should fall in the range between the rotational diffusion time $t_{\mathrm{rod}}(L)$ of a rigid rod of contour length L and $t_{\mathrm{rod}}(2L)$, the time for a rigid rod of length $2L$. Analytically, $t_{\mathrm{rod}}(L)$ can be approximated as follows (7):

$$t_{\mathrm{rod}}(L) = \frac{\pi\eta L^3}{3\ln(L/2d)}, \qquad \text{[S10]}$$

where η is the viscosity of water. The resulting rotational diffusion times $t_{\rm rod}(L)\approx 2.2$ μs and $t_{\rm rod}(2L)\approx 13.3$ μs are marked as black dashed lines in Fig. S2*A*, which establishes that $t_{\rm rod}(L)<t_{\rm r}<t_{\rm rod}(2L)$. A more precise analytical comparison can be made with the rotational diffusion time $t_{\rm w}$ of a structure consisting of two rigid rods of L connected by a flexible hinge, which has been estimated by Wegener (8):

$$t_{\rm w}(L)\approx 1.79\frac{\pi\eta L^3}{\ln(2L/d)}. \qquad \textbf{[S11]}$$

The resulting value, $t_{\rm w}(L)=4.6$ μs, which is marked as a red dashed line in Fig. S2*A*, is in good agreement with the simulation results. With a load force F applied to MyoV, the equilibrium position of the end point after detachment is shifted closer to the initial binding site. As a result, the relaxation times become shorter, as seen in Fig. S2*B*. In all cases, $t_{\rm r}$ is at least two orders of magnitude smaller than the typical first passage times to the binding site, which is consistent with the approximation used to derive Eq. **S9**.

Binding Probabilities. When MyoV is in the waiting state, with both heads bound to ADP and strongly associated with actin, we can have one of two scenarios for initiating a diffusive search: (I) ADP is released from the trailing head (TH) and quickly replaced by ATP, leading to the dissociation of the TH from actin, in which this detachment through ADP release/ATP binding has a overall rate of $t_{\rm d1}^{-1}$, and (II) less frequently, the leading head (LH) detaches without ADP release, which occurs at a rate of $t_{\rm d2}^{-1}\ll t_{\rm d1}^{-1}$. The gating parameter $g=t_{\rm d2}/t_{\rm d1}\gg 1$ describes the probabilities of the two scenarios occurring, which are $g(1+g)^{-1}$ for I and $(1+g)^{-1}$ for II.

Let us consider scenario I, which can lead either to a forward step if the TH rebinds to $\mathbf{r}_+$ or to a trailing foot stomp if the TH binds to $\mathbf{r}_-$. Denote the probabilities of these two binding events as $\mathcal{P}_{\rm f}$ and $\mathcal{P}_{\rm Ts}$. For the TH to bind to actin, three conditions must be fulfilled:

i) The TH must hydrolyze ATP, which occurs at a hydrolysis rate of $t_{\rm h}^{-1}$.
ii) Subsequently, the TH must reach the capture radius a of one of the binding sites. For $\mathbf{r}_+$, it reaches the capture radius with a rate of $(t_{\rm fp}^{+})^{-1}$ and then binds. For $\mathbf{r}_-$, it reaches the capture radius with a rate of $(t_{\rm fp}^{-})^{-1}$, but binding will only occur with probability b, reflecting the penalty for wrong head orientation after the recovery stroke. Thus, the effective rate of capture at the backward site is $b(t_{\rm fp}^{-})^{-1}$ with $b\ll 1$ (Table 1).
iii) During the entire diffusive search, the LH must not detach from actin or the entire MyoV structure will dissociate from the filament and the run is terminated. The detachment rate, assumed to be ATP-independent, is given by $t_{\rm d1}^{-1}$.

Requirements *i* and *ii* by themselves, and the assumption that individual events are Poisson-distributed, lead to probability distributions $f_{\rm Tb}^{\pm}(t)$ for the TH binding time to the $\mathbf{r}_\pm$ target sites:

$$\begin{aligned} f_{\rm Tb}^{+}(t) &= \int_0^t dt'\, t_{\rm h}^{-1}e^{-t'/t_{\rm h}}\left(t_{\rm fp}^{+}\right)^{-1}e^{-(t-t')\left[\left(t_{\rm fp}^{+}\right)^{-1}+b\left(t_{\rm fp}^{-}\right)^{-1}\right]} \\ &= \frac{e^{-t/t_{\rm h}}-e^{-t(1+b\alpha)/t_{\rm fp}^{+}}}{t_{\rm h}(1+b\alpha)-t_{\rm fp}^{+}}, \end{aligned} \qquad \textbf{[S12]}$$

$$\begin{aligned} f_{\rm Tb}^{-}(t) &= \int_0^t dt'\, t_{\rm h}^{-1}e^{-t'/t_{\rm h}}b\left(t_{\rm fp}^{-}\right)^{-1}e^{-(t-t')\left[\left(t_{\rm fp}^{+}\right)^{-1}+b\left(t_{\rm fp}^{-}\right)^{-1}\right]} \\ &= b\alpha f_{\rm Tb}^{+}(t), \end{aligned} \qquad \textbf{[S13]}$$

where $\alpha=t_{\rm fp}^{+}/t_{\rm fp}^{-}$. The integrals in Eq. **S12** are convolutions of the probability that hydrolysis occurs at some time t' and the probability of subsequent capture at a target site after a time interval $t-t'$. The average time to bind, $t_{\rm Tb}$, is the same for both sites:

$$t_{\rm Tb}=\frac{\int_0^\infty dt'\, t' f_{\rm Tb}^{+}(t')}{\int_0^\infty dt'\, f_{\rm Tb}^{+}(t')}=\frac{\int_0^\infty dt'\, t' f_{\rm Tb}^{-}(t')}{\int_0^\infty dt'\, f_{\rm Tb}^{-}(t')}=t_{\rm h}+\frac{t_{\rm fp}^{+}}{1+b\alpha}. \qquad \textbf{[S14]}$$

Using Eq. **S12**, it is straightforward to incorporate requirement *iii* and derive the probabilities $\mathcal{P}_{\rm f}$ and $\mathcal{P}_{\rm Ts}$:

$$\mathcal{P}_{\rm f}=\frac{g}{1+g}\int_0^\infty dt\, e^{-t/t_{\rm d1}}f_{\rm Tb}^{+}(t)=\frac{g}{1+g}\frac{t_{\rm d1}^2}{(1+b\alpha)(t_{\rm d1}+t_{\rm h})(t_{\rm d1}+t_{\rm Tb}-t_{\rm h})}. \qquad \textbf{[S15]}$$

$$\mathcal{P}_{\rm Ts}=\frac{g}{1+g}\int_0^\infty dt\, e^{-t/t_{\rm d1}}f_{\rm Tb}^{-}(t)=b\alpha\mathcal{P}_{\rm f}. \qquad \textbf{[S16]}$$

In scenario II, ATP hydrolysis is not required for rebinding, because the detached LH retains ADP and is in a state that can strongly associate with actin. The head orientation is now favorable for binding to the backward site, so the binding penalty b exists for $\mathbf{r}_+$ instead of $\mathbf{r}_-$. The free LH can bind to $\mathbf{r}_+$, a leading foot stomp with probability $\mathcal{P}_{\rm Ls}$, or it can bind to $\mathbf{r}_-$, a backward step with probability $\mathcal{P}_{\rm b}$. The LH analogs to Eqs. **S12**–**S16** can be obtained from these equations by the substitutions $t_{\rm h}=0$, $b(t_{\rm fp}^{-})^{-1}\to(t_{\rm fp}^{-})^{-1}$, and $(t_{\rm fp}^{+})^{-1}\to b(t_{\rm fp}^{+})^{-1}$. The results are

$$f_{\rm Lb}^{+}(t)=b\left(t_{\rm fp}^{+}\right)^{-1}e^{-t(b+\alpha)/t_{\rm fp}^{+}}, \qquad \textbf{[S17]}$$

$$f_{\rm Lb}^{-}(t)=b^{-1}\alpha f_{\rm Lb}^{+}(t), \qquad \textbf{[S18]}$$

$$t_{\rm Lb}=\frac{t_{\rm fp}^{+}}{b+\alpha}, \qquad \textbf{[S19]}$$

$$\mathcal{P}_{\rm Ls}=\frac{1}{1+g}\frac{bt_{\rm d1}}{(b+\alpha)(t_{\rm d1}+t_{\rm Lb})}, \qquad \textbf{[S20]}$$

$$\mathcal{P}_{\rm b}=b^{-1}\alpha\mathcal{P}_{\rm Ls}. \qquad \textbf{[S21]}$$

The final kinetic pathway, termination by complete dissociation from actin, occurs when the diffusive search in any of the four pathways above cannot be completed before the bound leg detaches. The termination probability is $\mathcal{P}_{\rm t}=1-\mathcal{P}_{\rm f}-\mathcal{P}_{\rm Ts}-\mathcal{P}_{\rm Ls}-\mathcal{P}_{\rm b}$.

From Eqs. **S15**, **S16**, **S20**, and **S21**, one can derive the pathway probability ratios shown in Eq. **4**. The results for the ratios have been simplified under the assumption that $t_{\rm d1}\gg t_{\rm Lb}, t_{\rm Tb}$, which is generally valid.

Average Step Shape. For comparison with the experiment of Dunn and Spudich (9), we will consider the average step trajectory $\langle\delta z(t)\rangle$ of the TH along $\hat{\mathbf{z}}$ after detachment from actin, where $\delta z(t)\equiv z(t)-z(0)$ and the initial position is the backward binding site, $z(0)=\hat{\mathbf{z}}\cdot\mathbf{r}_-=-\Delta$. In the ensemble of all possible trajectories at time t after detachment (with at least one head bound to actin), there will be two subpopulations: those trajectories where the TH is still unbound and those where the TH has bound either to the backward site $\mathbf{r}_-$ or to the forward site $\mathbf{r}_+$. In this calculation, we ignore the small fraction of trajectories that lead

to complete dissociation of the motor because these are not counted as completed steps, and hence do not contribute to the experimental measurement of $\langle \delta z(t) \rangle$. The fraction $\mathcal{P}^{\pm}_{\mathrm{Tb}}(t)$ of TH trajectories that has bound to $\mathbf{r}_{\pm}$ by time t is

$$\mathcal{P}^{+}_{\mathrm{Tb}}(t) = \int_0^t dt' \; f^{+}_{\mathrm{Tb}}(t') = \frac{t_{\mathrm{h}}\left(1-e^{-t/t_{\mathrm{h}}}\right) - t^{+}_{\mathrm{fp}}(1+b\alpha)^{-1}\left(1-e^{-t(1+b\alpha)/t^{+}_{\mathrm{fp}}}\right)}{t_{\mathrm{h}}(1+b\alpha) - t^{+}_{\mathrm{fp}}}, \quad \text{[S22]}$$

$$\mathcal{P}^{-}_{\mathrm{Tb}}(t) = \int_0^t dt' \; f^{-}_{\mathrm{Tb}}(t') = b\alpha \mathcal{P}^{+}_{\mathrm{Tb}}(t), \quad \text{[S23]}$$

where $f^{\pm}_{\mathrm{Tb}}(t)$ are the binding time distributions given by Eqs. **S12** and **S13**. The expression for the average step is then

$$\langle \delta z(t) \rangle = (\mu_z + \Delta)\left(1 - \mathcal{P}^{+}_{\mathrm{Tb}}(t) - \mathcal{P}^{-}_{\mathrm{Tb}}(t)\right)\left(1-e^{-t/t_{\mathrm{r}}}\right) + 2\Delta \mathcal{P}^{+}_{\mathrm{Tb}}(t). \quad \text{[S24]}$$

The first term in Eq. **S24** reflects the relaxation of the unbound subpopulation over a characteristic time t_{r} to the average position of the free end along the $\hat{\mathbf{z}}$ axis, $\mu_z = \langle \hat{\mathbf{z}} \cdot \mathbf{r} \rangle$, where $\mathbf{r}$ is the end-to-end vector of MyoV, and the average is taken over the equilibrium configurations of a two-legged polymer with one leg bound to the actin filament and the other leg free. As described in the next section, this average can be exactly derived and is related to the structural parameters of the system: the leg contour length L, the persistence length l_p, the strength of the end-tangent constraint ν_c at the bound end, and the angle of the constraint direction θ_c relative to the $\hat{\mathbf{z}}$ axis. The full expression for μ_z is

$$\mu_z = l_p\left(1-e^{-L/l_p}\right)\left(\coth \nu_c - \nu_c^{-1}\right)\cos\theta_c. \quad \text{[S25]}$$

For those interested in the derivation, $\mu_z = \mu_{\parallel}^{\mathrm{exact}} \cos\theta_c$, where $\mu_{\parallel}^{\mathrm{exact}}$ is given by Eq. **S38** below. The value of the polymer relaxation time is $t_{\mathrm{r}} \approx 5$ μs, as discussed above. The second term in Eq. **S24** is the contribution of trajectories that have bound to $\mathbf{r}_{+}$, and hence covered a distance of $\delta z = 2\Delta$ along the filament axis. Trajectories binding to the initial site $\mathbf{r}_{-}$ have $\delta z = 0$, and so do not appear in Eq. **S24**.

Run Length and Velocity. If the termination probability during each diffusive search is $\mathcal{P}_{\mathrm{t}} = 1 - \mathcal{P}_{\mathrm{f}} - \mathcal{P}_{\mathrm{Ts}} - \mathcal{P}_{\mathrm{Ls}} - \mathcal{P}_{\mathrm{b}}$, then the mean number of searches during a run is $\sum_{n=1}^{\infty} n(1-\mathcal{P}_{\mathrm{t}})^{n-1}\mathcal{P}_{\mathrm{t}} = 1/\mathcal{P}_{\mathrm{t}}$. The fraction of the searches within a run that leads to forward steps is $\mathcal{P}_{\mathrm{f}}/(1-\mathcal{P}_{\mathrm{t}})$, and the fraction that leads to backward steps is $\mathcal{P}_{\mathrm{b}}/(1-\mathcal{P}_{\mathrm{t}})$. The mean run length, assuming step size Δ, is given by

$$z_{\mathrm{run}} = \frac{\Delta\left(\mathcal{P}_{\mathrm{f}} - \mathcal{P}_{\mathrm{b}}\right)}{\mathcal{P}_{\mathrm{t}}(1-\mathcal{P}_{\mathrm{t}})} \approx \frac{\Delta t_{\mathrm{d1}}\left(\alpha(g-1) + b\left(g-\alpha^2\right)\right)}{(b+\alpha)(1+b\alpha)(t_{\mathrm{Lb}} + g t_{\mathrm{Tb}})}, \quad \text{[S26]}$$

where we have used the pathway probabilities from Eqs. **S15**, **S16**, **S20**, and **S21** in the limit $t_{\mathrm{d1}} \gg t_{\mathrm{Lb}}, t_{\mathrm{Tb}}$.

The mean velocity is $v_{\mathrm{run}} = z_{\mathrm{run}}/t_{\mathrm{run}}$, where t_{run} is the average run time. To calculate the latter, we note that the mean waiting period (when both heads are bound to actin) is $t_{\mathrm{d1}}t_{\mathrm{d2}}/(t_{\mathrm{d1}} + t_{\mathrm{d2}}) = g t_{\mathrm{d1}}/(1+g)$, whereas the mean binding times for the TH/LH are t_{Tb} (Eq. **S14**) and t_{Lb} (Eq. **S19**), respectively. Then, t_{run} for $t_{\mathrm{d1}} \gg t_{\mathrm{Lb}}, \; t_{\mathrm{Tb}}$ is given by

$$t_{\mathrm{run}} = \frac{\mathcal{P}_{\mathrm{f}} + \mathcal{P}_{\mathrm{Ts}}}{\mathcal{P}_{\mathrm{t}}(1-\mathcal{P}_{\mathrm{t}})}\left(\frac{g}{1+g}t_{\mathrm{d1}} + t_{\mathrm{Tb}}\right) + \frac{\mathcal{P}_{\mathrm{b}} + \mathcal{P}_{\mathrm{Ls}}}{\mathcal{P}_{\mathrm{t}}(1-\mathcal{P}_{\mathrm{t}})}\left(\frac{g}{1+g}t_{\mathrm{d1}} + t_{\mathrm{Lb}}\right) \approx \frac{g t_{\mathrm{d1}}^2}{t_{\mathrm{Lb}} + g t_{\mathrm{Tb}}}, \quad \text{[S27]}$$

where the first term is the contribution of steps involving TH detachment and the second term is the contribution of those involving LH detachment. The resulting expression for v_{run} is

$$v_{\mathrm{run}} = \frac{z_{\mathrm{run}}}{t_{\mathrm{run}}} \approx \frac{\Delta}{t_{\mathrm{d1}}}\left(\frac{1}{1+b\alpha} - \frac{\alpha}{g(b+\alpha)}\right). \quad \text{[S28]}$$

Eqs. **S26**–**S28** are reproduced as Eq. **9**.

3. Equilibrium Probability of Myosin End-Point Fluctuations

The equilibrium probability $\mathcal{P}(\mathbf{r})$ of finding the MyoV free end at position $\mathbf{r}$ (Fig. S3), needed to calculate t^{+}_{fp} in Eq. **S9**, can be obtained from calculating the end-to-end vector probabilities of the bound leg, $\mathcal{P}_b(\mathbf{r}_b)$, and the free leg, $\mathcal{P}_f(\mathbf{r}_f)$. Because $\mathbf{r}$ is the sum of the end-to-end vectors of the legs, $\mathbf{r} = \mathbf{r}_b + \mathbf{r}_f$, $\mathcal{P}(\mathbf{r})$ can be written as a convolution of the two leg probabilities:

$$\mathcal{P}(\mathbf{r}) = \int d\mathbf{r}_b \int d\mathbf{r}_f \; \mathcal{P}_b(\mathbf{r}_b)\mathcal{P}_f(\mathbf{r}_f)\delta(\mathbf{r} - \mathbf{r}_b - \mathbf{r}_f). \quad \text{[S29]}$$

Each leg is an inextensible semiflexible polymer of contour length L and persistence length l_p (10), and one end of the bound leg is fixed at the origin $\mathbf{r} = 0$. The bound leg has two energetic contributions not present for the free leg: (*i*) the tangent vector of the bound leg at the origin, $\hat{\mathbf{u}}_0$, is subject to a harmonic constraint with energy $\mathcal{H}_c = \frac{1}{2}k_BT\nu_c(\hat{\mathbf{u}}_0 - \hat{\mathbf{u}}_c)^2$, where ν_c and $\hat{\mathbf{u}}_c$ are the strength and direction of the angle constraint, respectively ($\hat{\mathbf{v}}$ denotes a unit vector, meaning $|\hat{\mathbf{v}}| = 1$), and (*ii*) a load force $\mathbf{F}$ is applied at the other end of the bound leg, where it joins the free leg. The force is oriented at an angle θ_F clockwise from the $-\hat{\mathbf{z}}$ axis, as shown in Fig. S3. The axis $\hat{\mathbf{z}}$ is oriented from the minus to plus end of the actin filament. Both of these energetic contributions will lead to an overall tension in the bound leg that has to be accounted for in calculating the probability $\mathcal{P}_b(\mathbf{r}_b)$. In the following subsections, we present approximate analytical expressions for the leg probabilities $\mathcal{P}_f(\mathbf{r}_f)$ and $\mathcal{P}_b(\mathbf{r}_b)$, justifying them by comparison with exact results for the first and second moments of the equilibrium probabilities. In the final subsection, we take the individual leg results and use Eq. **S29** to derive a complete analytical expression for $\mathcal{P}(\mathbf{r})$, which is needed to calculate the first passage times (Eq. **S9**).

Equilibrium End-to-End Probability of the Free Leg. We start with the simpler case of the free leg, which is not under tension. There is no exact closed form analytical expression for the end-to-end vector probability $\mathcal{P}_f(\mathbf{r}_f)$ of a semiflexible polymer [although the moments of the probability distribution are known analytically (10, 11), as illustrated below]. Mean field theory, however, provides an excellent approximation of the distribution (12):

$$\mathcal{P}_f(\mathbf{r}_f) = A_f \xi_f^{-9/2} \exp\left(-\frac{3\kappa}{4\xi_f}\right), \quad \text{[S30]}$$

where $\kappa = L/l_p$ and $\xi_f = 1 - r_f^2/L^2$, and A_f is a normalization constant. The end-to-end vector $\mathbf{r}_f$ can be specified by the polar and azimuthal angles θ_f and ϕ_f, as well as by the dimensionless radial variable ξ_f, which can only take on values between 0 and 1 for an inextensible polymer, because $r_f \le L$. In this coordinate system, the normalization condition for the probability is

$$1=\frac{L^3}{2}\int_0^1 d\xi_f(1-\xi_f)^{1/2}\int_0^\pi d\theta_f\int_0^{2\pi} d\phi_f\ \mathcal{P}_f(\mathbf{r}_f). \qquad \text{[S31]}$$

The normalization constant A_f is given by

$$A_f=\frac{9\sqrt{3}e^{3\kappa/4}\kappa^{7/2}}{8\pi^{3/2}L^3(3\kappa^2+12\kappa+20)}. \qquad \text{[S32]}$$

In the stiff limit of large persistence length ($\kappa\to 0$), the probability in Eq. **S30** goes to a delta function at $r_f=L$, as is appropriate for a rigid rod of L. In the opposite limit of flexible chains ($\kappa\to\infty$), the probability goes to a Gaussian centered at $\mathbf{r}=0$. Throughout the entire range of κ, the second moment of the probability distribution, $\langle r_f^2\rangle=2L^2(3\kappa+10)/(3\kappa^2+12\kappa+20)$, is within 1% of the exact result $\langle r_f^2\rangle_{\text{exact}}=2L^2\kappa^{-2}(\kappa-1+e^{-\kappa})$ (10, 11). (The first moment $\langle\mathbf{r}_f\rangle$ is trivially equal to zero in both the exact and approximate cases because of the radial symmetry of the distribution.) The approximation of Eq. **S30** thus captures the physical features of the stiff and flexible limits and is reasonably accurate for our purposes.

Equilibrium End-to-End Probability of the Bound Leg at Zero Load. We first consider the bound leg in the absence of load on the joint ($F=0$). Our expression for $\mathcal{P}_b(\mathbf{r}_b)$ should reduce to the free leg probability of Eq. **S30** in the limit of zero constraint strength $\nu_c=0$. For $\nu_c\neq 0$, we assume the effect of the end-tangent constraint can be approximated by the following ansatz:

$$\mathcal{P}_b(\mathbf{r}_b)=A_b\xi_b^{-9/2}\exp\left(-\frac{3\kappa}{4\xi_b}+\mathcal{T}\ \hat{\mathbf{u}}_c\cdot\hat{\mathbf{r}}_b\right), \qquad \text{[S33]}$$

where $\xi_b=1-r_b^2/L^2$, A_b is a normalization constant, and $\mathcal{T}$ is an unknown function of ν_c to be determined later, satisfying $\mathcal{T}=0$ at $\nu_c=0$. Eq. **S33** is identical in form to Eq. **S30**, except for the additional $\mathcal{T}$ term in the exponential, which acts as an effective tension along $\hat{\mathbf{u}}_c$ due to the end-tangent constraint. The normalization constant A_b is given by

$$A_b=A_f\frac{\mathcal{T}}{\sinh\mathcal{T}}. \qquad \text{[S34]}$$

We choose $\mathcal{T}$ so that the first and second moments of the probability distribution of Eq. **S33** closely agree with the exact values for a semiflexible polymer under a harmonic end-tangent constraint. Because the analytical expressions for these exact values are not available in the literature, we derive them in the following way. We start by noting that the bound leg end-to-end vector $\mathbf{r}_b=\int_0^L ds\hat{\mathbf{u}}(s)$, where $\hat{\mathbf{u}}(s)=d\mathbf{r}(s)/ds$ is the tangent vector at position s along the bound leg chain contour $\mathbf{r}(s)$, $0\le s\le L$. The tangent vectors for an inextensible chain all have unit length. The equilibrium statistics of $\hat{\mathbf{u}}(s)$ for a semiflexible polymer are governed by the Green's function $G(\hat{\mathbf{u}},\hat{\mathbf{u}}';s-s')$, which describes the probability that a chain with tangent vector $\hat{\mathbf{u}}(s)=\hat{\mathbf{u}}$ will have tangent vector $\hat{\mathbf{u}}(s')=\mathbf{u}'$ at some position $s'\ge s$. This Green's function has an exact spherical harmonic expansion of the form (11)

$$G(\hat{\mathbf{u}},\hat{\mathbf{u}}';s-s')=\sum_{l,m}e^{-\frac{l(l+1)}{2l_p}(s'-s)}Y_{lm}^*(\hat{\mathbf{u}})Y_{lm}(\hat{\mathbf{u}}'). \qquad \text{[S35]}$$

For the initial tangent vector $\hat{\mathbf{u}}_0\equiv\hat{\mathbf{u}}(0)$ at $s=0$, where the bound leg is attached to the actin, the harmonic constraint leads to a probability distribution $\mathcal{P}_c(\hat{\mathbf{u}}_0)$ given by

$$\begin{aligned}\mathcal{P}_c(\hat{\mathbf{u}}_0)&=\frac{\nu_c}{2\pi(1-e^{-2\nu_c})}\exp\left(-\frac{\nu_c}{2}(\hat{\mathbf{u}}_0-\hat{\mathbf{u}}_c)^2\right)\\&=\sqrt{\frac{\pi\nu_c}{2}}\ \frac{1}{\sinh\nu_c}\sum_{l,m}I_{l+1/2}(\nu_c)Y_{lm}^*(\hat{\mathbf{u}}_c)Y_{lm}(\hat{\mathbf{u}}_0).\end{aligned} \qquad \text{[S36]}$$

In the first line, the prefactor in front of the exponential is a normalization constant. In the second line, we have rewritten the exponential in a spherical harmonic expansion (13) involving modified spherical Bessel functions of the first kind $I_\nu(x)$. This form will facilitate carrying out the moment integrals below.

Let $\hat{\mathbf{t}}$ be one of the three orthogonal unit vectors $\hat{\mathbf{u}}_c$, $\hat{\mathbf{v}}_c$, or $\hat{\mathbf{w}}_c$, as defined in Fig. S3. These axes, with $\hat{\mathbf{u}}_c$ being the constraint direction, are the easiest to work with for moment calculations. Using the definitions of $G(\hat{\mathbf{u}},\hat{\mathbf{u}}';s-s')$ and $\mathcal{P}_c(\hat{\mathbf{u}}_0)$ above, the first- and second-order moments with respect to one of the axes $\hat{\mathbf{t}}$ can be written as

$$\begin{aligned}\left\langle\hat{\mathbf{t}}\cdot\mathbf{r}_b\right\rangle_{\text{exact}}&=\left\langle\int_0^L ds\ \hat{\mathbf{t}}\cdot\hat{\mathbf{u}}(s)\right\rangle_{\text{exact}}\\&=\int_0^L ds\int d\hat{\mathbf{u}}_0\int d\hat{\mathbf{u}}\mathcal{P}_c(\hat{\mathbf{u}}_0)G(\hat{\mathbf{u}}_0,\hat{\mathbf{u}}';s)\ \hat{\mathbf{t}}\cdot\hat{\mathbf{u}},\\\left\langle(\hat{\mathbf{t}}\cdot\mathbf{r}_b)^2\right\rangle_{\text{exact}}&=\left\langle\int_0^L ds\int_0^L ds'\ \hat{\mathbf{t}}\cdot\hat{\mathbf{u}}(s)\hat{\mathbf{t}}\cdot\hat{\mathbf{u}}(s')\right\rangle_{\text{exact}}\\&=2\int_0^L ds\int_s^L ds'\int d\hat{\mathbf{u}}_0\int d\hat{\mathbf{u}}\int d\hat{\mathbf{u}}'\\&\quad\mathcal{P}_c(\hat{\mathbf{u}}_0)G(\hat{\mathbf{u}}_0,\hat{\mathbf{u}};s)\ \hat{\mathbf{t}}\cdot\hat{\mathbf{u}}G(\hat{\mathbf{u}},\hat{\mathbf{u}}';s'-s)\hat{\mathbf{t}}\cdot\hat{\mathbf{u}}'.\end{aligned} \qquad \text{[S37]}$$

By using Eqs. **S35** and **S36** and the properties of spherical harmonics, the integrals in Eq. **S37** can be carried out exactly to yield the moments for any axis $\hat{\mathbf{t}}$. Let us define the average end-to-end component parallel to the constraint direction, $\mu_\parallel^{\text{exact}}\equiv\langle\hat{\mathbf{u}}_c\cdot\mathbf{r}_b\rangle_{\text{exact}}$ (the first moments along $\hat{\mathbf{v}}_c$ and $\hat{\mathbf{w}}_c$ are zero). Similarly, define the parallel and perpendicular end-to-end SDs, $\sigma_\parallel^{\text{exact}}\equiv\left(\left\langle(\hat{\mathbf{u}}_c\cdot\mathbf{r}_b)^2\right\rangle_{\text{exact}}-\langle\hat{\mathbf{u}}_c\cdot\mathbf{r}_b\rangle_{\text{exact}}^2\right)^{1/2}$ and $\sigma_\perp^{\text{exact}}\equiv\left\langle(\hat{\mathbf{v}}_c\cdot\mathbf{r}_b)^2\right\rangle_{\text{exact}}^{1/2}=\left\langle(\hat{\mathbf{w}}_c\cdot\mathbf{r}_b)^2\right\rangle_{\text{exact}}^{1/2}$. The results for these three quantities are

$$\begin{aligned}\mu_\parallel^{\text{exact}}&=L\kappa^{-1}(1-k)\mathcal{L}(\nu_c),\\\sigma_\parallel^{\text{exact}}&=\frac{L\kappa^{-1}}{3}\left(2(3\kappa+k^3-1)-9(k-1)^2\mathcal{L}^2(\nu_c)-\frac{6(k+2)(k-1)^2\mathcal{L}(\nu_c)}{\nu_c}\right)^{1/2},\\\sigma_\perp^{\text{exact}}&=\frac{L\kappa^{-1}}{3}\left(6\kappa-k^3+9k-8+\frac{3(k^3-3k+2)\mathcal{L}(\nu_c)}{\nu_c}\right)^{1/2},\end{aligned} \qquad \text{[S38]}$$

where $k\equiv\exp(-\kappa)$ and $\mathcal{L}(\nu_c)\equiv\coth\nu_c-\nu_c^{-1}$ is the Langevin function.

The corresponding moments calculated from the probability distribution in Eq. **S33** are

$$\begin{aligned}\mu_\parallel&=\frac{L\mathcal{L}(\mathcal{T})}{\sqrt{\pi}\left(\frac{9}{4}\kappa(\kappa+4)+15\right)}\left(\frac{3\sqrt{\pi}(10-3\kappa)}{2k^{3/4}}\operatorname{erfc}\frac{\sqrt{3\kappa}}{2}+3\sqrt{3\kappa}(\kappa+5)\right),\\\sigma_\parallel&=L\kappa^{-1}\left(\frac{2\kappa^2(3\kappa+10)(\mathcal{T}-2\mathcal{L}(\mathcal{T}))}{(3\kappa(\kappa+4)+20)\mathcal{T}}-\frac{\mu_\parallel^2}{L^2}\right)^{1/2},\\\sigma_\perp&=L\kappa^{-1}\left(\frac{2\kappa^2(3\kappa+10)\mathcal{L}(\mathcal{T})}{(3\kappa(\kappa+4)+20)\mathcal{T}}\right)^{1/2}.\end{aligned} \qquad \text{[S39]}$$

To determine $\mathcal{T}$, we will set $\mu_\parallel$ from Eq. **S39** equal to $\mu_\parallel^{\text{exact}}$ from Eq. **S38**. The resulting expression for $\mathcal{T}$ is

$$\mathcal{T}=\mathcal{L}^{-1}\left(\frac{\sqrt{\pi}(3\kappa(\kappa+4)+20)(1-k)k^{3/4}\mathcal{L}(\nu_c)}{2\kappa\left(\sqrt{\pi}(10-3\kappa)\mathrm{erfc}\left(\frac{\sqrt{3\kappa}}{2}\right)+2\sqrt{3\kappa}(\kappa+5)k^{3/4}\right)}\right). \quad [S40]$$

Because the inverse Langevin function $\mathcal{L}^{-1}(x)$ cannot be expressed analytically, for the purposes of evaluation, we use the Padé approximation $\mathcal{L}^{-1}(x)\approx x(3-x^2)/(1-x^2)$ (14). For the parameter regimes $\kappa\ll 1$ (large stiffness) and $\nu_c\gg 1$ (strong end-tangent constraint), relevant to MyoV dynamics, Eq. **S40** can be further simplified to yield

$$\mathcal{T}\approx 1+\frac{20\nu_c}{20+7\kappa\nu_c}. \quad [S41]$$

Eqs. **S33**, **S34**, and **S41** completely describe the end-to-end vector probability distribution for the bound leg at zero load. By construction, the $\mathcal{T}$ of Eq. **S41** leads to a $\mu_\parallel$ that closely agrees with the exact value $\mu_\parallel^{\text{exact}}$ from Eq. **S38**. In addition, the other moments are reproduced well by the approximate probability distribution, as shown in Fig. S4. The exact and approximate values differ by no more than 7% over the entire parameter range of l_p and ν_c. This range covers the most likely parameters for MyoV dynamics, as discussed in the main text.

Equilibrium End-to-End Probability of the Bound Leg Under Load. In the presence of a load force $\mathbf{F}$, the probability distribution in Eq. **S33** is multiplied by a factor of $\exp(\beta F r_b\hat{\mathbf{F}}\cdot\hat{\mathbf{r}}_b)=\exp(\beta FL(1-\xi_b)^{1/2}\hat{\mathbf{F}}\cdot\hat{\mathbf{r}}_b)$. In the stiff limit $\kappa\ll 1$, the main contributions to the end-to-end vector probability are for $\xi_b\ll 1$, because r_b approaches L, the leg contour length. Thus, the contribution of the load can be approximated as $\exp(\beta FL\hat{\mathbf{F}}\cdot\hat{\mathbf{r}}_b)$. With this approximation, the overall form of Eqs. **S33** and **S34** is preserved under load, with the substitutions $\mathcal{T}\to\mathcal{T}'$ and $\hat{\mathbf{u}}_c\to\hat{\mathbf{u}}_c'$. The probability distribution becomes

$$\mathcal{P}_b(\mathbf{r}_b)=A_b\xi_b^{-9/2}\exp\left(-\frac{3\kappa}{4\xi_b}+\mathcal{T}'\,\hat{\mathbf{u}}_c'\cdot\hat{\mathbf{r}}_b\right), \quad [S42]$$

$$A_b=A_f\frac{\mathcal{T}'}{\sinh\mathcal{T}'}, \quad [S43]$$

where the new effective tension along the leg, written in terms of its $\hat{\mathbf{x}}$ and $\hat{\mathbf{z}}$ components, is

$$\mathcal{T}'=\sqrt{(\mathcal{T}_x')^2+(\mathcal{T}_z')^2},\quad \mathcal{T}_x'=\mathcal{T}\sin\theta_c+\beta FL\sin\theta_F,\quad \mathcal{T}_z'=\mathcal{T}\cos\theta_c-\beta FL\cos\theta_F. \quad [S44]$$

The new effective tension direction is $\hat{\mathbf{u}}_c'=\sin\theta_c'\hat{\mathbf{x}}+\cos\theta_c'\hat{\mathbf{z}}$, which is oriented at an angle θ_c' from the $\hat{\mathbf{z}}$ axis:

$$\theta_c'=\theta_c+\tan^{-1}\left(\frac{\beta FL\sin(\theta_c+\theta_F)}{\mathcal{T}-\beta FL\cos(\theta_c+\theta_F)}\right). \quad [S45]$$

Combining the Individual Leg Probabilities to Find the Total End-to-End Vector Probability Distribution. The final step in the derivation of $\mathcal{P}(\mathbf{r})$ is to evaluate Eq. **S29**. Using $\mathcal{P}_f$ from Eq. **S30** and $\mathcal{P}_b$ from Eq. **S42**, the convolution integral in Eq. **S29** has the form

$$\begin{aligned}\mathcal{P}(\mathbf{r})&=A_fA_b\int d\mathbf{r}_b\int d\mathbf{r}_f\;\xi_f^{-9/2}\xi_b^{-9/2}\exp\left(-\frac{3\kappa}{4\xi_f}-\frac{3\kappa}{4\xi_b}+\mathcal{T}'\,\hat{\mathbf{u}}_c'\cdot\hat{\mathbf{r}}_b\right)\delta(\mathbf{r}-\mathbf{r}_b-\mathbf{r}_f)\\&=A_fA_b\int d\mathbf{r}_b\;\xi_f^{-9/2}\xi_b^{-9/2}\exp\left(-\frac{3\kappa}{4\xi_f}-\frac{3\kappa}{4\xi_b}+\mathcal{T}'\,\hat{\mathbf{u}}_c'\cdot\hat{\mathbf{r}}_b\right).\end{aligned} \quad [S46]$$

In the second step, we have carried out the integration over the free leg end-to-end vector $\mathbf{r}_f$, with the delta function making the radial variable $\xi_f=1-r_f^2/L^2$ a function of $\mathbf{r}$ and $\mathbf{r}_b$:

$$\xi_f=1-\frac{r^2+r_b^2-2rr_b\cos\theta_b}{L^2}, \quad [S47]$$

where θ_b is the angle between $\mathbf{r}$ and $\mathbf{r}_b$. Because we are interested in probabilities of finding the free end of MyoV along the actin filament, let us confine the rest of the calculation to $\mathbf{r}=z\hat{\mathbf{z}}$, where $-2L\le z\le 2L$ (because this is the maximum range that the two-legged structure of total contour length $2L$ can access). The unit vector $\hat{\mathbf{r}}_b$ can be represented in spherical coordinates by the polar and azimuthal angles (θ_b,ϕ_b), and $\hat{\mathbf{u}}_c'$ can be represented by $(\theta_c',\phi_c'=0)$. Thus,

$$\hat{\mathbf{u}}_c'\cdot\hat{\mathbf{r}}_b=\cos\theta_b\cos\theta_c'+\cos\phi_b\sin\theta_b\sin\theta_c'. \quad [S48]$$

Writing the integration element in Eq. **S46** as $d\mathbf{r}_b=r_b^2d\cos\theta_bd\phi_b$, we can carry out the integral over ϕ_b using Eq. **S48**. The result is

$$\begin{aligned}\mathcal{P}(z\hat{\mathbf{z}})=2\pi A_fA_b\int_0^L r_b^2dr_b\int_{-1}^1 d\cos\theta_b\;\xi_f^{-9/2}\xi_b^{-9/2}\\\times\exp\left(-\frac{3\kappa}{4\xi_f}-\frac{3\kappa}{4\xi_b}+\mathcal{T}_z'\cos\theta_b\right)\cdot I_0(\mathcal{T}_x'\sin\theta_b),\end{aligned} \quad [S49]$$

where $I_0(x)$ is the zeroth-order modified Bessel function of the first kind. To simplify the integration, we will change variables from $(r_b,\cos\theta_b)$ to (ξ_b,ξ_f). From the definitions of ξ_b and ξ_f, and from Eq. **S47**, the two sets of variables are related by

$$r_b=L\sqrt{1-\xi_b},\quad \cos\theta_b=\frac{z^2+L^2(\xi_f-\xi_b)}{2zL\sqrt{1-\xi_b}}, \quad [S50]$$

leading to a Jacobian determinant $|\det J|=L^2/(4|z|(1-\xi_b))$ for the change of variables. Using these relations, Eq. **S49** becomes

$$\begin{aligned}\mathcal{P}(z\hat{\mathbf{z}})=\frac{L^4\,\pi A_fA_b}{2|z|}\int_0^{u_b(z)}d\xi_b\int_0^{u_f(z,u_b)}d\xi_f\;\xi_f^{-9/2}\xi_b^{-9/2}\\\cdot\exp\left(-\frac{3\kappa}{4\xi_f}-\frac{3\kappa}{4\xi_b}+\mathcal{T}_z'\frac{z^2+L^2(\xi_f-\xi_b)}{2zL\sqrt{1-\xi_b}}\right)\\\cdot I_0\left(\mathcal{T}_x'\sqrt{1-\left(\frac{z^2+L^2(\xi_f-\xi_b)}{2zL\sqrt{1-\xi_b}}\right)^2}\right),\end{aligned} \quad [S51]$$

where the upper limits of integration are given by

$$u_b(z)=\frac{2|z|}{L}-\frac{z^2}{L^2},\quad u_f(z,\xi_b)=\xi_b+\frac{2|z|\sqrt{1-\xi_b}}{L}-\frac{z^2}{L^2}. \qquad \textbf{[S52]}$$

In the stiff limit $\kappa\to 0$, the main contributions to the integral come from $\xi_b \ll 1$ and $\xi_f \ll 1$. Additionally, the location of the binding sites we consider, $|z|=36$ nm, is comparable to the leg contour length $L=35$ nm. We can then approximately carry out the integral in Eq. **S51** by replacing the integration limits $u_b\to 1$ and $u_f\to 1$, and by substituting

$$\frac{z^2+L^2(\xi_f-\xi_b)}{2zL\sqrt{1-\xi_b}}\to\frac{z}{2L}. \qquad \textbf{[S53]}$$

With these approximations, the integral in Eq. **S51** evaluates to

$$\mathcal{P}\left(z\hat{\mathbf{z}}\right)\approx\frac{8\pi L^4 A_f A_b}{729\kappa^7|z|}\left(20\sqrt{3\pi}e^{3\kappa/4}\operatorname{erfc}\left(\frac{\sqrt{3\kappa}}{2}\right)+3\sqrt{\kappa}(\kappa(3\kappa+10)+20)\right)^2 \cdot I_0\left(\mathcal{T}'_x\sqrt{1-\frac{z^2}{4L^2}}\right)e^{\frac{1}{2}\left(\frac{\mathcal{T}'z}{L}-3\kappa\right)}. \qquad \textbf{[S54]}$$

Upon substituting in Eq. **S32** for A_f and in Eq. **S43** for A_b, and upon expanding $\mathcal{P}(z\hat{\mathbf{z}})$ up to the second order in κ, we get the final simplified form of the probability. The result evaluated at $z=\pm\Delta$ is given by Eq. **20**:

$$\mathcal{P}(\mathbf{r}_\pm)\approx\frac{(3\kappa(7\kappa+20)+200)\mathcal{T}'}{1,600\pi L^2\Delta\sinh\mathcal{T}'}I_0\left(\mathcal{T}'_x\sqrt{1-\frac{\Delta^2}{4L^2}}\right)e^{\pm\frac{\mathcal{T}'\Delta}{2L}}. \qquad \textbf{[S55]}$$

Together with Eq. **S41** for $\mathcal{T}$ and Eq. **S44** for $\mathcal{T}'$, we now have a complete analytical expression for the probability distribution of the MyoV free end at any location along the actin filament axis.

An analogous approach can be used to find $\mathcal{P}(\mathbf{r})$ analytically at any $\mathbf{r}$ and not just along $\hat{\mathbf{z}}$. The resulting 3D probability distribution allows us to generate sample diffusive trajectories for the end-to-end vector $\mathbf{r}$ in various MyoV kinetic pathways, as shown in Fig. S5. These are numerical solutions to the Fokker–Planck equation (15) for diffusion along an energy surface $U(\mathbf{r})=-k_BT\log\mathcal{P}(\mathbf{r})$ with head diffusivity D_h.

4. Stall Force

Based on the earlier results for the step probabilities and first passage times, one can derive a simple expression for the stall force F_{stall}, defined by the condition that backward and forward step probabilities are equal, $\mathcal{P}_\text{f}=\mathcal{P}_\text{b}$ at $F=F_{\text{stall}}$. From Eqs. **S15** and **S21**, the ratio of the two probabilities is

$$\frac{\mathcal{P}_\text{b}}{\mathcal{P}_\text{f}}=\frac{\alpha(1+b\alpha)(t_{\text{d1}}+t_\text{h})(t_{\text{d1}}+t_{\text{Tb}}-t_\text{h})}{g(b+\alpha)t_{\text{d1}}(t_{\text{d1}}+t_{\text{Lb}})}\approx g^{-1}\frac{\alpha(1+b\alpha)}{b+\alpha}. \qquad \textbf{[S56]}$$

The approximation in the second line is valid when $t_{\text{d1}}\gg t_{\text{Tb}},\ t_{\text{Lb}}$, which is typically the case.

Setting the right-hand side of Eq. **S56** equal to 1, we can solve for the value $\alpha=\alpha_{\text{stall}}$ at the stall force:

$$\alpha_{\text{stall}}=\frac{g-1+\sqrt{(g-1)^2+4gb^2}}{2b}. \qquad \textbf{[S57]}$$

Using Eq. **S9** for $t_{\text{fp}}^{\pm}$, Eq. **S55** for the equilibrium free end probability $\mathcal{P}(\mathbf{r}_\pm)$, and the definition of $\mathcal{T}'$ from Eq. **S44**, we can rewrite Eq. **S57** as follows:

$$\frac{g-1+\sqrt{(g-1)^2+4gb^2}}{2b}=\alpha_{\text{stall}}=\left.\frac{\mathcal{P}(\mathbf{r}_-)}{\mathcal{P}(\mathbf{r}_+)}\right|_{F=F_{\text{stall}}} =\exp\left(-\frac{\Delta\mathcal{T}}{L}\cos\theta_c+\beta\Delta F_{\text{stall}}\cos\theta_F\right). \qquad \textbf{[S58]}$$

This equation can be directly solved for F_{stall}, giving Eq. **10**:

$$F_{\text{stall}}=\frac{k_BT}{\cos\theta_F}\left(\frac{\mathcal{T}}{L}\cos\theta_c+\frac{1}{\Delta}\log\frac{g-1+\sqrt{(g-1)^2+4gb^2}}{2b}\right). \qquad \textbf{[S59]}$$

1. van Kampen NG (2007) *Stochastic Processes in Physics and Chemistry* (North-Holland, Amsterdam), 3rd ed.
2. Coureux PD, Sweeney HL, Houdusse A (2004) Three myosin V structures delineate essential features of chemo-mechanical transduction. *EMBO J* 23(23):4527–4537.
3. Ortega A, Amorós D, García de la Torre J (2011) Prediction of hydrodynamic and other solution properties of rigid proteins from atomic- and residue-level models. *Biophys J* 101(4):892–898.
4. Guo Z, Thirumalai D (1995) Kinetics of protein folding: Nucleation mechanism, time scales, and pathways. *Biopolymers* 36(1):83–102.
5. Ermak DL, McCammon JA (1978) Brownian dynamics with hydrodynamic interactions. *J Chem Phys* 69(4):1352–1360.
6. Rotne J, Prager S (1969) Variational treatment of hydrodynamic interaction in polymers. *J Chem Phys* 50(11):4831–4837.
7. Doi M, Edwards SF (1988) *The Theory of Polymer Dynamics* (Oxford Univ Press, New York).
8. Wegener WA (1980) Hydrodynamic resistance and diffusion-coefficients of a freely hinged rod. *Biopolymers* 19(10):1899–1908.
9. Dunn AR, Spudich JA (2007) Dynamics of the unbound head during myosin V processive translocation. *Nat Struct Mol Biol* 14(3):246–248.
10. Kratky O, Porod G (1949) Rontgenuntersuchung geloster fadenmolekule. *Recueil Des Travaux Chimiques Des Pays Bas* 68:1106–1122, Dutch.
11. Saito N, Takahashi W, Yunoki Y (1967) Statistical mechanical theory of stiff chains. *J Phys Soc Jpn* 22:219–226.
12. Thirumalai D, Ha BY (1998) *Theoretical and Mathematical Methods in Polymer Research*, ed Grosberg AY (Academic, New York), pp 1–35.
13. Chiu LYC, Moharerrzadeh M (1994) Translational and rotational expansion of spherical gaussian wave-functions for multicenter molecular integrals. *J Chem Phys* 101(1):449–458.
14. Cohen A (1991) A pade approximant to the inverse Langevin function. *Rheol Acta* 30: 270–273.
15. Wang HY, Peskin CS, Elston TC (2003) A robust numerical algorithm for studying biomolecular transport processes. *J Theor Biol* 221(4):491–511.

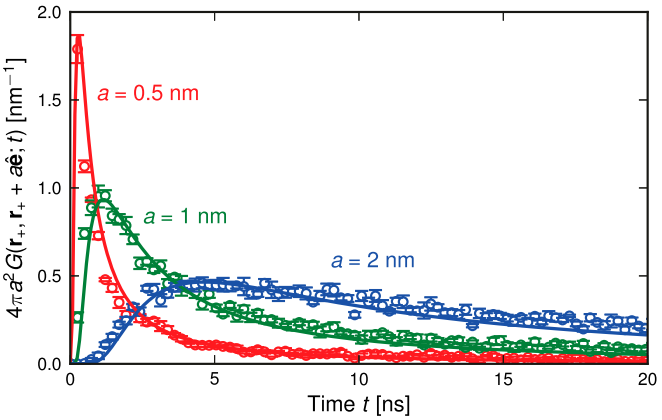

Fig. S1. Brownian dynamics simulation results (circles) for the Green's functions of the end point of the two-legged MyoV structure, with $\nu_c = 184$, $l_p = 310$ nm, and $\theta_c = 60^\circ$. The plot shows $4\pi a^2 G(\mathbf{r}_+, \mathbf{r}_+ + a\hat{\mathbf{e}}; t)$ as a function of time t, where $G(\mathbf{r}_+, \mathbf{r}_+ + a\hat{\mathbf{e}}; t)$ is the probability of diffusing a distance a from $\mathbf{r}_+$ to some point $\mathbf{r}_+ + a\hat{\mathbf{e}}$, with $|\hat{\mathbf{e}}| = 1$. Results for three different values of a are displayed: $a = 0.5$ nm (red), $a = 1$ nm (green), and $a = 2$ nm (blue). Error bars denote SE for the simulation-derived values. For comparison, the solid curves represent the expression $4\pi a^2 (4\pi D t)^{-3/2} \exp(-a^2/(4Dt))$, the right-hand side of Eq. **S7** multiplied by $4\pi a^2$, with a best-fit value of $D = 1.4 \pm 0.1 \times 10^{-6}$ cm^2/s.

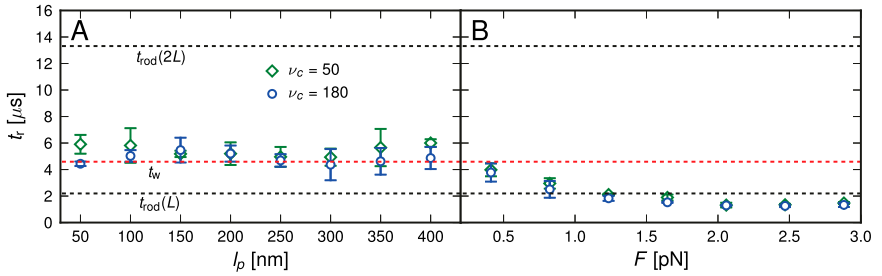

Fig. S2. Relaxation times t_r for the trailing end point of the two-legged MyoV structure to reach equilibrium after detachment, calculated from Brownian dynamics simulations. Results are shown at two different strengths $\nu_c = 50$, 180 of the bound leg power stroke constraint with $\theta_c = 60^\circ$. (*A*) Relaxation times t_r at zero load as a function of leg persistence length l_p. (*B*) Relaxation times t_r at $l_p = 310$ nm as a function of backward load force F. For comparison, three analytically estimated rotational diffusion times are shown as horizontal dashed lines: $t_{rod}(L)$ and $t_{rod}(2L)$ (black) (Eq. **S10**) for a rigid rod of L and $2L$, respectively, and $t_w(L)$ (red) (Eq. **S11**) for two rigid rods of L connected at a flexible hinge.

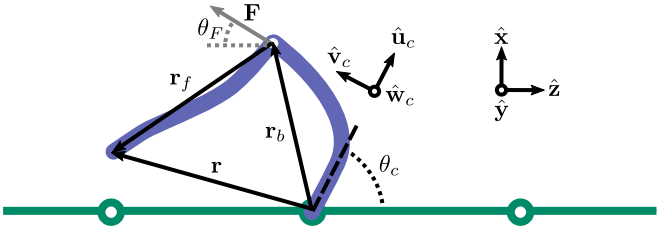

Fig. S3. Schematic diagram for the polymer model of MyoV, defining the free end-point vector $\mathbf{r}$ and the end-to-end vectors for the free $(\mathbf{r}_f)$ and bound $(\mathbf{r}_b)$ legs, respectively. The unit vector $\hat{\mathbf{u}}_c$ is the direction of the end-tangent constraint on the bound leg, and together with the two orthogonal unit vectors $\hat{\mathbf{v}}_c$ and $\hat{\mathbf{w}}_c$ it forms a set of axes tilted at an angle θ_c from the $(\hat{\mathbf{x}}, \hat{\mathbf{y}}, \hat{\mathbf{z}})$ axes, where $\hat{\mathbf{z}}$ is oriented along the actin filament.

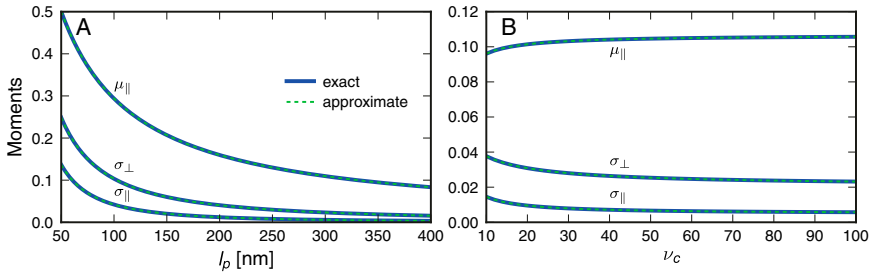

Fig. S4. First and second moments of the end-to-end vector distribution for the bound leg when $\mathbf{F}=0$, measured in units of leg persistence length l_p. The exact values (solid lines) are given by Eq. **S38**, whereas the approximate values (dashed lines) are taken from Eq. **S39**, with $\mathcal{T}$ defined by Eq. **S41**. (*A*) Moments as a function of persistence length l_p for fixed constraint strength $\nu_c = 180$. (*B*) Moments as a function of ν_c for fixed $l_p = 310$ nm.

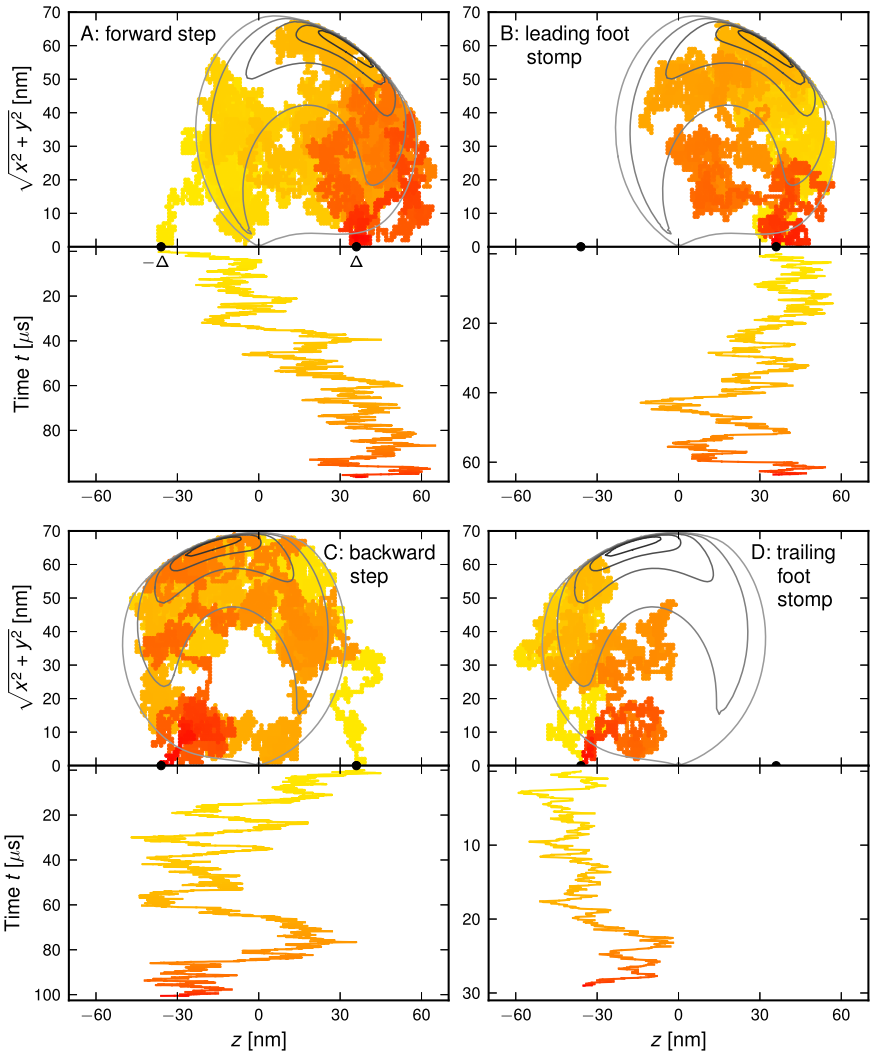

Fig. S5. Sample trajectories of the end-to-end vector $\mathbf{r}=(x,y,z)$ for each of the four MyoV kinetic pathways, calculated from a numerical solution (15) to the Fokker–Planck equation with head diffusivity D_h and an energy landscape $U(\mathbf{r}) = -k_BT\log\mathcal{P}(\mathbf{r})$, with $\mathcal{P}(\mathbf{r})$ given by Eq. **S46**. (*Upper*) Trajectories in terms of z (the distance along actin) vs. $\sqrt{x^2+y^2}$, with colors from yellow to red denoting progress in time, are shown for each pathway. (*Lower*) Corresponding $z(t)$ for the trajectory, using the same color-coding, is shown. (*Upper*) Superimposed are contour lines of $\mathcal{P}(\mathbf{r})$ for probabilities $1,2,\ldots,5\cdot10^{-4}$ nm^{-3} (light gray to dark gray). The pathways in *A* and *B* are at $F=0$ pN, whereas those in *C* and *D* are at $F=2$ pN ; hence, the $\mathcal{P}(\mathbf{r})$ distribution in the latter cases is shifted in the $-\hat{\mathbf{z}}$ direction.